Koç University

Graduate School of Sciences and Engineering

This is to certify that I have examined this copy of a master's thesis by

Işınsu Baylam

and have found that it is complete and satisfactory in all respects,
and that any and all revisions required by the final
examining committee have been made.

Committee Members:

_____

Alphan Sennaroğlu, Ph. D. (Advisor)

_____

Kaan Güven, Ph. D.

_____

Sarper Özharar, Ph. D.

Date: _____

ABSTRACT

In mode-locking applications, single-walled carbon nanotube saturable absorbers (SWCNT-SAs) and graphene saturable absorbers (graphene-SAs) have emerged as important alternatives to semiconductor saturable absorber mirrors (SESAMs) due to their favorable optical characteristics, low cost, and relatively simple fabrication scheme. Therefore, it is of great interest to explore the limits of energy scaling in lasers mode-locked with SWCNT-SAs and graphene-SAs.

In this thesis work, due to their unique wavelength range for biomedical applications, a room-temperature Cr^{4+}: forsterite laser operating near 1.3 μm was used in the mode-locking experiments. By incorporating a q-preserving multi-pass cavity (MPC) extension to the short x-cavity, an effective optical path length of ~ 60 m was obtained and the repetition rate of the pulses was reduced to 4.51 MHz from 144 MHz. In addition, by using double chirped (DCM) and Gires-Tournois interferometer (GTI) mirrors, nonlinear phase distortions due to self phase modulation were compensated to generate solitary femtosecond pulses. Furthermore, the power efficiency of different laser resonator architectures containing the graphene-SA or SWCNT-SA was investigated.

The Cr^{4+}: forsterite laser, mode-locked with a SWCNT-SA produced 121-fs pulses with 10-nJ pulse energy and 84-kW peak power at the wavelength of 1247 nm. The mode-locked spectrum had a width of 16 nm, corresponding to a time-bandwidth product of 0.37. Hence, the pulses were nearly transform-limited with a temporal profile of $sech^2$.

For graphene-SA mode-locking experiments, graphene samples with different number of layers were fabricated and characterized. The Cr^{4+}: forsterite laser mode-locked with a single layer graphene-SA produced 96-fs pulses with 5.3-nJ pulse energy and 55-kW peak power at 1252 nm. In this case, the mode-locked spectrum had a width of 18.2 nm and the

measured time-bandwidth product came to 0.33, also indicating that nearly transform limited solitary pulses were generated.

To our knowledge, both of the results report the highest peak powers obtained to date from a femtosecond solid-state bulk laser mode locked by using SWCNT-SA and graphene-SA. Limitations to energy scaling were further explored during the experiments.

ÖZET

Karbon nanotüp ve grafen tabanlı doyabilen soğurucular optik özellikleri ve diğer yarı-iletken malzemelere kıyasla düşük üretim maliyetine sahip olmaları nedeniyle, yarı-iletken doyabilen soğurucu aynalara (SESAM) alternatif olarak kip-kilitleme (mode-locking) deneylerinde kullanılmaya başlanmıştır. Bu nedenle, karbon nanotüp ve grafen tabanlı doyabilen soğurucular kullanılarak kip-kilitli rejimde çalıştırılan lazerlerin enerjilerinin ölçeklendirme limitlerini araştırmak, bu soğurucuların yüksek güce sahip lazerlerle uyumluluğunu anlamak açısından oldukça önemlidir.

Bu çalışmamızda, çok yansımalı kovuk içeren bir Cr^{4+}: forsterite lazeri kullanarak, karbon nanotüp ve grafen soğurucuların daha yüksek enerjili lazerlerde de kullanılabileceğini deneysel olarak gösterdik. Deneyler için 1.3 μm civarında çalışan ve biyomedikal görüntülemede birçok potansiyel uygulamaları bulunan bir Cr^{4+}: forsterite lazeri tercih edilmiştir. Rezonatörün boyunu uzatmak ve aynı zamanda darbe enerjisini arttırmak için, lazer içerisine çok yansımalı, q parametresini koruyan bir optik kovuk (q-preserving multi-pass cavity) ilave edilmiştir. Çok yansımalı kovuk sayesinde, lazerin uzunluğu 60 m civarına arttırılıp, darbe tekrar frekansı 144 MHz civarından 4.51 MHz'e indirilmiştir. Soliton darbeleri üretebilmek için, rezonatöre eksi dispersiyona sahip aynalar (DCM ve GTI) ilave edilmiştir. Bunlara ek olarak, karbon nanotüp ve grafen soğurucuları içeren farklı resonator tasarımları için lazerin verimliliği araştırılmıştır.

Karbon nanotüp tabanlı doyabilen soğurucu yardımıyla kip-kilitli rejimde çalıştırılan Cr^{4+}: forsterite lazeri, 1247 nm dalga boyunda, darbe enerjisi 10 nj civarında, 84 kW darbe tepe gücüne sahip ve uzunluğu 121 fs olan darbeler üretmiştir. 16 nm spectral kalınlığı ile elde edilen darbe-spektral kalınlık çarpımı 0.37 civarındadır. Bu sonuç, üretilen darbe profilinin yaklaşık olarak $sech^2$ şeklinde olduğunu göstermektedir.

Grafen tabanlı doyabilen soğurucu ile yapılan kip-kilitleme deneyleri için farklı kalınlıklara sahip grafen örnekleri sentezlenmiştir ve bu örneklerin karakterizasyonu yapılmıştır. Tek katmana sahip grafen tabanlı soğurucu örneği kullanılarak, Cr^{4+}: forsterite lazeri kip-kilitli rejimde çalıştırılmıştır. Cr^{4+}: forsterite lazerinden, 1252 nm'de çalışan, darbe enerjisi 5.3 nJ civarında, 55 kW darbe tepe gücüne sahip ve darbe uzunluğu 96 fs olan darbeler üretilmiştir. 18.2 nm spectral kalınlığa karşılık gelen darbe-spektral kalınlık çarpımı 0.33 civarındadır ve bu deneylerin sonucunda da soliton darbelerin üretilmiş olduğunu göstermektedir.

Her iki deney sonucunda da elde edilen darbe tepe gücü değerleri, karbon nanotüp ve grafen tabanlı soğurucular ile kip-kilitli rejimde çalıştırılan femtosaniye katı-hal lazerleri için şimdiye kadar elde edilebilen en yüksek tepe gücü değerleridir.

Bu çalışma sonucunda, karbon nanotüp ve grafen tabanlı doyabilen soğurucuların da yüksek enerjili darbe üretimi için elverişli olduğu gösterilmiştir ve enerji ölçeklendirilmesini limitleyen faktörler detaylı olarak araştırılmıştır.

ACKNOWLEDGMENTS

During my master study and my thesis work, lots of people motivated me and inspired me. In this part of my thesis, I would like to present my appreciation to them.

First of all, I would like to thank my advisor Alphan Sennaroğlu for giving me the opportunity to study in the Laser Research Laboratory under his supervision. He was always willing to share his knowledge and experience with me. I feel very lucky about continuing my further education in his laboratory because I believe that there is plenty of additional advice which I should learn from him to become an academician who is complete in every respect.

Second, I would like to thank Adnan Kurt. He broadened my way of thinking and my philosophy of life with his incredible amount of original ideas and his technical and non-technical advice. I gained different points of views from the discussions that I made with him. I will continue to observe his experimental skills in the laboratory and I will continue to ask my questions to him to learn more from his experience and ideas.

I also would like to thank Sarper Özharar for his educational and friendly collaboration. I am pretty sure that he will train many qualified researchers. I was very lucky to work with him because I could ask him whatever I did not know about physics and academic life. Also, it was a perfect coincidence to me that both of us were into the Star Wars and science fiction so that we sometimes procrastinated together while discussing about the details of the characters and settings during our coffee breaks.

I am very grateful about the friendly environment of our laboratory which is a result of the harmony between all of us. I would like to thank Ferda Canbaz, Devrim Köseoğlu, İsmail Yorulmaz, Ersen Beyatlı, Philipp Heck and our undergraduate students Cem Yetişmişoğlu and Merve Şahin for their friendship and help during my thesis work. Especially, I present my deepest appreciation to Hüseyin Çankaya and Natali Çizmeciyan

for their support during my master study. They never hesitated to help me and I learned many things from their laboratory experience.

Kaan Güven is one of the best instructors that I met in Koç University. I would like to thank him as my thesis committee member and my instructor. His valuable comments will improve my research.

I would also like to thank my house-mates Ayşen Sarıoğlu, Mine Toker and Tuğba Nur Öztürk for all the enjoyable and peaceful days we spent together. In addition to them, I would like to thank my friends Mustafa Eryürek, Enis Doko, and Güneş Aydındoğan for their friendship during my master study.

In addition to wonderful people I met in Koç University, I would like to thank my undergraduate senior project advisors F. Ömer İlday and Coşkun Kocabaş for their guidance during my undergraduate study. I decided to learn more about lasers and laser optics after the optics course that F. Ömer İlday taught us. I was always inspired by both of my advisors' dedication, motivation, and energy. I also thank Coşkun Kocabaş for helping me, in his laboratory, in the fabrication of the graphene samples that I used in my experiments.

I am sincerely thankful that I met Erçağ Pinçe. I would like to thank him for his endless support, patience and love for the past three years that we spent together.

Last but not least, I would like to thank my mother Neriman Baylam and my father Erdem Baylam. My love and my appreciation to them are beyond words. I would like to dedicate my thesis to them.

TABLE OF CONTENTS

LIST OF FIGURES

NOMENCLATURE

$\propto$:	fine structure constant
$\propto_L$:	differential loss coefficient
$\propto_T$:	total differential loss coefficient
A:	area / absorption / element of the ray transformation matrix
A_{eff}.:	effective area
A_{21}:	Einstein's A coefficient for spontaneous emission
B:	Brightness / element of the ray transformation matrix
B_{12}:	Einstein's B coefficient for absorption
B_{21}:	Einstein's B coefficient for stimulated emission
c:	speed of light in vacuum
C:	element of the ray transformation matrix
d:	distance
d_g:	length of the gain medium
D:	group delay dispersion parameter / element of the ray transformation matrix
e:	electron charge
E:	energy / energy level
E_{gap}:	band-gap energy
E_{sat}:	saturation energy
f:	focal length
$f_{rep:}$	repetition rate of the pulses
g:	ground state energy level
$g_{T:}$	maximum extractable small-signal gain
G:	gain
G_0:	small-signal fractional gain

h:	Planck's constant
I:	light intensity
I_L:	laser intensity
I_p:	pump intensity
I_{sat}:	saturation intensity
$\mathbf{k}$:	wave vector
K:	time-bandwidth product
l_c:	coherence length
L:	total loss of the resonator
L_c:	cavity length
L_{eff}:	effective optical path length
M:	M-square parameter / mirror
n:	refractive index
n_0:	low intensity refractive index
n_2:	nonlinear refractive index
n_g:	population density of the ground state
N:	population density
γ:	Kerr nonlinearity (self-phase modulation) constant
γ_0:	small-signal gain coefficient
$\gamma_{12}(\tau)$:	mutual coherence function
ε_0:	permittivity of free space
η:	slope efficiency
η_a:	fractional pump absorption
θ_i:	incident angle
λ_L:	laser wavelength
λ_p:	pump wavelength

$\Delta\nu$:	bandwidth
ν_L	laser frequency
ν_p:	pump frequency
ν_F:	Fermi velocity
ν_{FSR}:	free spectral range
q:	q-paramater of the beam
Q:	Q-factor of the cavity
P:	power
P_{cr}:	critical power
R:	reflectivity
$\boldsymbol{\rho}$:	ray vector
σ_a:	absorption cross section
σ_e:	emission cross section
τ_c:	coherence time
τ_f:	fluorescene lifetime
τ_p:	pulse width / cavity photon lifetime
T:	transmission
u_g:	group velocity
ϕ:	phase
Ω:	solid-angle
ω:	angular frequency
w(z):	spotsize function
w_0:	beam waist
z_0:	Rayleigh range

Chapter 1

INTRODUCTION

In this part of the thesis, a brief history of lasers will be given and the important physical concepts underlying optical amplification will be described. Part 1.2 discusses the gain mechanism, stimulated and spontaneous emission, and oscillation condition for lasers. Expressions for the threshold pump power and slope efficiency of a laser are also given. In Part 1.3, general information and historical review of Cr^{4+}: forsterite lasers will be presented.

1.1 Historical Review and Theoretical Background of Lasers

The fundamental physical theory of optical amplification (i.e. stimulated emission) which describes the operation of lasers was first established by Albert Einstein in 1917. Then, studies that led to an operational laser were performed by several scientists including Arthur Leonard Schawlow, Charles Hard Townes, Nikolay Basov, and Alexander Prokhorov. In 1960, the first operating laser was reported by Theodore Maiman [1]. Today, lasers have widespread applications in biomedicine [2-4], communication systems [5], astronomical imaging [6], product development [7], and industrial systems [8].

In its simplest configuration, a laser consists of a gain medium for optical amplification and two highly reflecting mirrors which provide positive feedback. According to the physical characteristics of the gain medium, lasers can be classified as gas, liquid or solid-state

lasers. In this thesis, the main focus will be on solid-state lasers and discussion about other gain medium types will not be undertaken.

1.2.1 Optical Processes of Stimulated Absorption, Spontaneous Emission and Stimulated Emission

To understand the optical interactions in an optical gain medium, it is important to first describe the absorption and emission processes. As is well known from Quantum Theory, microscopic systems like atoms and molecules consist of discrete energy levels. The interaction of this medium with light can be understood by assuming that light consists of photons, each with an energy of

$$E = h\nu \tag{1.2.1}$$

where, h is the Planck's constant and ν is the frequency of the photon. Interaction of light with an ideal two-level atomic system results in absorption and subsequent transition of atoms from the lower ground level $|1\rangle$ (E_1) to an upper level $|2\rangle$ (E_2) as shown in Fig. 1.2.1.

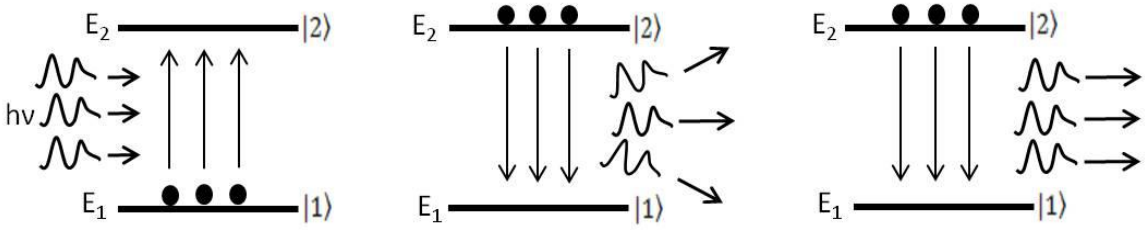

Figure 1.2.1 *Schematics for* ***(a)*** *stimulated absorption,* ***(b)*** *spontaneous emission, and* ***(c)*** *stimulated emission processes, respectively.*

The atomic density of the upper level is designated as N_2 and according to Einstein's model, the time rate of change of N_2 is given by

$$\frac{dN_2}{dt} = N_1 B_{12} \int_0^\infty d\nu \rho(\nu) g(\nu) \, . \tag{1.2.2}$$

Here, g(ν) is the lineshape function, ρ(ν) is spectral energy density, and B_{12} is the Einstein's B coefficient for absorption. N_2 and N_1 are the atomic densities for levels $|2\rangle$ and $|1\rangle$, respectively. Since people use other laser sources to excite a crystal gain medium, we can assume that interacting light is monochromatic at the frequency ν. As a result, the spectral width becomes much smaller than the lineshape function. Therefore, the spectral energy density at frequency ν' can be approximated as

$$\rho(\nu') = \rho_\nu \delta(\nu' - \nu). \tag{1.2.3}$$

If we rewrite Eq. (1.2.2), we obtain

$$\frac{dN_2}{dt} = B_{12} N_1 \int_0^\infty d\,\nu' \rho_\nu \delta(\nu' - \nu) g(\nu') \, . \tag{1.2.4}$$

By using the translation property of the delta function

$$\int f(x') \, \delta(x' - x) dx' = f(x) \tag{1.2.5}$$

the rate equation for stimulated absorption simplifies to [9]

$$\frac{dN_2}{dt} = B_{12}N_1\rho_\nu g(\nu). \tag{1.2.6}$$

As a result of this interaction, both stimulated emission and spontaneous emission occur at the same time. Figure 1.2.1 shows the schematic description for stimulated and spontaneous emission. As seen from Fig. 1.2.1, for spontaneous emission, photons are emitted in random directions and with random phases. On the other hand, in the case of stimulated emission, emitted photons have the same direction, polarization, frequency, and phase.

In the case of spontaneous emission, due to the vacuum fluctuations of the quantized electromagnetic field, atoms in the upper level can decay to the lower level without incident stimulating photons. This decay rate is given by

$$\left(\frac{dN_2}{dt}\right)_{radiative} = -A_{21}N_2\,. \tag{1.2.7}$$

In this equation, similar to Eq. (1.2.2), A_{21} describes the transition process from energy level $|2\rangle$ to $|1\rangle$ and it is called the Einstein's A coefficient for spontaneous emission. However, in real systems there are also non-radiative decay processes which result in the generation of heat in the host medium. Hence, the overall decay rate can be written as

$$\frac{dN_2}{dt} = -\frac{N_2}{\tau_f}\,. \tag{1.2.8}$$

Where τ_f is the fluorescence lifetime and is given in terms of the radiative and non-radiative decay components ($W_{non\text{-}rad.}$) as

$$\tau_f = \frac{1}{A_{21}+W_{non-rad.}} \ . \tag{1.2.9}$$

In the case of the stimulated emission, if the atom interacts with photons having the frequency

$$h\nu \cong E_2 - E_1 \tag{1.2.10}$$

excited atoms are stimulated to undergo a downward transition to the lower level by emitting photons with the same energy, phase, polarization, and direction. Hence, this leads to optical gain and is the fundamental optical process which initiates laser operation. The rate of this process can be written as

$$\frac{dN_2}{dt} = -B_{21}N_2 \int_0^\infty d\nu\rho(\nu)g(\nu). \tag{1.2.11}$$

If we use the same argument as in Eq. (1.2.3), the stimulated emission rate becomes [9]

$$\frac{dN_2}{dt} = -B_{21}N_2\rho_\nu g(\nu). \tag{1.2.12}$$

Similarly, B_{21} describes transitions from energy level $|2\rangle$ to energy level $|1\rangle$ and it is called the Einstein's B coefficient for stimulated emission. The minus sign in Eq. (1.2.7) and Eq. (1.2.12) shows that both spontaneous emission and stimulated emission cause a decrease in the upper-state population density.

1.2.2 Gain Mechanism

If the upper-state population of an atom exceeds the lower level population, we get a non-equilibrium condition known as population inversion and optical amplification occurs in the gain medium. For solid-state lasers, this medium is typically a laser-active ion-doped insulating crystal. In our experiments, the forsterite (Mg_2SiO_4) single crystal doped with Cr^{4+} ion was used. Usually, rare earth ions (e.g. Nd, Tm, Er) or transition metal ions (e.g. Cr^{4+}, Ni^{2+}, Ti^{3+}) are used for doping various types of hosts. Different types of host and ion combinations result in emissions at different wavelengths of the electromagnetic spectrum. Chemical properties and laser characteristics of Cr^{4+}: forsterite crystal will be investigated in Part 1.3. Now, to understand the gain mechanism behind lasers, it is important to put emphasis on the rate equation analysis for the solid-state gain medium. The population inversion is strongly related with the rates of stimulated emission and absorption. Since the four level atomic systems always have population inversion and the gain medium used in the experiments is a four level system, the rate equation analysis for a four level atomic system will be described in this section.

In Fig. 1.2.2, schematic description for absorption and stimulated emission in a four level system is described.

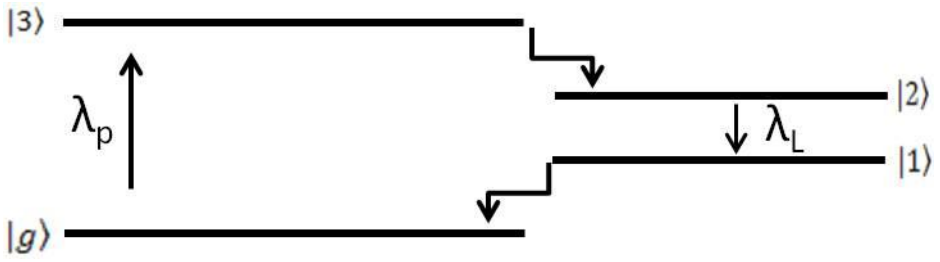

Figure 1.2.2 *Schematic description for the energy levels of a four level solid-state laser system.*

The optical pump photons at the wavelength λ_p are absorbed in the gain medium and excite atoms from the ground level $|g\rangle$ (E_g) to the upper energy level $|3\rangle$. Then, a rapid non-radiative decay occurs from $|3\rangle$ to the nearest lower energy level $|2\rangle$. Between $|2\rangle$ and $|1\rangle$, both spontaneous and stimulated emissions occur at the laser wavelength λ_L. Finally, ions at $|1\rangle$ rapidly go to $|g\rangle$ via non-radiative decay.

Since, the decay rates between levels$|3\rangle$-$|2\rangle$ and $|1\rangle$-$|g\rangle$ are fast compared to the transitions between $|g\rangle$-$|3\rangle$ and $|2\rangle$-$|1\rangle$, the population densities of the energy levels $|3\rangle$ and $|1\rangle$ are negligible (i.e. $N_3=N_1=0$). In addition, the photons emitted as a result of spontaneous emission will be neglected, because they will only add noise to the laser beam. Therefore, the overall rate equation becomes [9]

$$\frac{dN_2}{dt} = \frac{\sigma_a I_p}{h\nu_L} N_g - \frac{N_2}{\tau_f} - \frac{\sigma_e I_L}{h\nu_L} N_2 \ , \tag{1.2.13}$$

where, σ_a is the absorption cross section, σ_e is the emission cross section, and I_p, I_L are the pump and laser intensities respectively. If we further assume a gain medium with thickness of dz and area of A, we will obtain the following equality between the total number of photons added to the emission within this gain medium per unit time and the total number of ions that decay as a result of stimulated emission within the same volume per unit time as

$$\left(\frac{I_L(z+dz)-I_L(z)}{h\nu_L}\right) A = \left(\frac{\sigma_e I_L}{h\nu_L}\right) A dz \ . \tag{1.2.14}$$

If we define the total atomic density as

$$N_T = N_g + N_2 \ , \tag{1.2.15}$$

and the maximum extractable small-signal gain as

$$g_T = \sigma_e N_2 \,, \tag{1.2.16}$$

we can rewrite Eq. (1.2.14) in the following form

$$\frac{1}{I_L}\frac{dI_L}{dz} = g_T \frac{I_p}{I_{sa}} \frac{1}{1+\frac{I_p}{I_{sa}}+\frac{I_L}{I_{se}}} \,. \tag{1.2.17}$$

In this equation, I_{sa} and I_{se} are stimulated absorption and stimulated emission intensities, respectively. For very large pump intensities, the laser intensity will grow as light propagates in the gain medium. However, this growth is limited due to the gain saturation because of the finite number of atoms in the ground state energy level $|g\rangle$. To have a more realistic case, a loss coefficient (α_L) should also be subtracted from the right hand side of Eq. (1.2.17), because real systems always have losses originating from parasitic absorptions and scattering.

1.2.3 Oscillation Condition, Threshold Pump Power and Slope Efficiency of Lasers

As a result of light oscillation inside the resonator, lasers emit radiation at a specific wavelength. Optical amplification combined with positive feedback produces light oscillation. Optical amplification is the result of the gain mechanism discussed above and positive feedback is obtained via highly reflecting mirror configurations which form the optical cavity. There is a threshold pump power after which light starts to oscillate inside the cavity. When the oscillation condition is reached with sufficient pump power, lasing starts. In addition to this, to determine how much output power can be extracted with a

given pump power, the slope efficiency of the resonator should be calculated. Since, all of these concepts are closely related with the gain mechanism, the threshold pump power formula and the slope efficiency formula will be obtained based on the gain analysis. The fractional power gain (G) per pass through the gain medium can be defined as

$$G \equiv \frac{\Delta P_L}{P_L} . \tag{1.2.18}$$

Since the laser power can be written as $P_L = AI_L$, Eq. (1.2.18) can be rewritten

$$G = \frac{\Delta I_L A}{I_L A} . \tag{1.2.19}$$

By using Eq. (1.2.14) for ΔI_L, the fractional power gain per pass becomes

$$G = \sigma_e N_2 d_g . \tag{1.2.20}$$

Here, the short length of the gain medium (dz) is expressed as d_g. In order to find the differential equation for the power gain, Eq. (1.2.13) is multiplied by $\sigma_e d_g$ to have a similar expression with Eq. (1.2.20). Furthermore, if the pump absorption saturation is negligible, the differential equation for the power gain is obtained as [9]

$$\frac{dG}{dt} = -\frac{G(t)-G_0}{\tau_f} - \frac{P_L(t)G(t)}{E_{sat}} . \tag{1.2.21}$$

In Eq. (1.2.21), G_0 is the small-signal fractional power gain, and the saturation energy is given by

$$E_{sat} = \frac{h\nu_L}{\sigma_e} A \, . \tag{1.2.22}$$

In addition, the steady-state value for the fractional power gain can be found by setting the time derivative in Eq. (1.2.21) to zero, and is given by

$$G_s = \frac{G_0}{1+\frac{P_L}{P_{sat}}} , \tag{1.2.23}$$

where, P_{sat} is equal to E_{sat} divided by the fluorescence time τ_f, and is given by

$$P_{sat} = \frac{E_{sat}}{\tau_f} = \frac{h\nu_L}{\sigma_e \tau_f} A \, . \tag{1.2.24}$$

With the help of the plane wave analysis [9], the expression for the threshold pump power can be found. By denoting the beam power after m^{th} and $(m+1)^{th}$ round-trips as P_m and P_{m+1}, we obtain

$$P_{m+1} = P_m R_1 R_2 e^{-2\alpha_L d_g} = P_m e^{-2\alpha_T d_g} \, . \tag{1.2.25}$$

In this equation, α_T is the total differential loss coefficient and R_1, R_2 are the reflectivities of the end mirrors. Since the round-trip gain is unity at threshold, these parameters are related through the following equation:

$$\alpha_T = \alpha_L + \frac{1}{2d_g} ln\left(\frac{1}{R_1 R_2}\right) . \tag{1.2.26}$$

If the thickness of the gain medium is assumed to be small, the fractional change in the laser power after one round-trip becomes

$$\frac{\Delta P_L}{P_L} = -2\alpha_T d_g \,, \tag{1.2.27}$$

and can be rewritten as

$$\frac{dP_L}{dt} \approx \frac{\Delta P_L}{\Delta t} \,. \tag{1.2.28}$$

For Eq. (1.2.28), if we take the cavity length as L_c and c as the speed of light, Δt becomes

$$\Delta t = \frac{2L_c}{c} \,. \tag{1.2.29}$$

Thus, the change in the laser power after one round-trip becomes

$$\frac{dP_L}{dt} \approx -\frac{P_L}{\tau_p} \,. \tag{1.2.30}$$

τ_p is known as the cavity photon life-time and is given by [9]

$$\tau_p = \frac{2L_c/c}{2\alpha_L d_g + ln\left(\frac{1}{R_1 R_2}\right)} \,. \tag{1.2.31}$$

In order to complete the analysis, the optical gain should be added to the above discussion. Using Eq. (1.2.18), the change in the laser power after one round-trip is given by

$$\Delta P_L = 2GP_L\,, \tag{1.2.32}$$

and the differential equation for the laser power becomes

$$\frac{dP_L}{dt} = -\frac{P(t)}{\tau_p} + \frac{2G(t)}{T_R}P_L(t). \tag{1.2.33}$$

T_R is equal to the round-trip time of the cavity and is equal to:

$$T_R = \frac{2L_c}{c}\,. \tag{1.2.34}$$

Now, we have two coupled differential equations, namely Eqs. (1.2.21) and (1.2.33). If we set the time derivatives of these equations to zero, we obtain the threshold value of the fractional power gain [9]:

$$\frac{2G_{th}}{T_R} = \frac{1}{\tau_p}\,, \tag{1.2.35}$$

or

$$G_{th} = \frac{T_R}{2\tau_p} = \left[\alpha_L d_g + \frac{1}{2} ln\left(\frac{1}{R_1 R_2}\right)\right]. \tag{1.2.36}$$

In steady state, Eq. (1.2.23) will be equal to the value of the threshold gain. Thus, using the expression for P_{sat}, the output power can be written as

$$P_{out} = (1 - R_2)\frac{P_{sat}}{2}\left(\frac{G_0}{G_{th}} - 1\right). \tag{1.2.37}$$

There is a linear relationship between the output power and the small-signal gain coefficient (G_0). If the nonlinear effects are neglected, G_0 will increase as the pump power increases. As a result, the output power will also increase. By concentrating on the specific case where R_1 has perfect reflectivity (100%) and R_2 is equal to (1-T), where T is the transmission of the output coupler, the threshold gain becomes

$$G_{th} = \left[\alpha_L d_g + \frac{1}{2} ln\left(\frac{1}{1-T}\right)\right] \approx \frac{1}{2}[L + T]\,. \tag{1.2.38}$$

Here, $L = 2d_g\,\alpha_L$ is the total material loss in one cavity round-trip. As discussed before, the fractional power gain in steady state is proportional to the pump power. On this basis, it can be concluded like that, the threshold pump power required for lasing is [9]

$$\left(P_p\right)_{th} = A(L + T), \tag{1.2.39}$$

where A is a constant.

Using this formula, the passive losses in a laser cavity can be determined. The threshold pump power is measured as a function of output coupler transmission and the cavity loss is calculated easily by using Eq. (1.2.39). The final important concept for this section is the slope efficiency of the laser. The slope efficiency gives the change in the output power per unit increase in the input pump power. The formula for the slope efficiency η is given by

$$\eta = \frac{\Delta P_{out}}{\Delta P_p}. \tag{1.2.40}$$

By using Eq. (1.2.24), the formula for the slope efficiency can be rewritten as [9]

$$\eta = \frac{T\left(\frac{1}{2}\right)\frac{h\nu_L}{\sigma_e \tau_f} A \sigma_a n_g \sigma_e d_g \tau_f}{\frac{1}{2}(L+T)Ah\nu_p} = \frac{\lambda_p}{\lambda_L}\frac{T}{T+L}\eta_a \,. \tag{1.2.41}$$

In Eq. (1.2.41), n_g is the ground-state population density, and η_a is the fractional pump absorption given by

$$\eta_a = \sigma_a N_g d_g \approx \sigma_a N_T d_g \,. \tag{1.2.42}$$

From Eq. (1.2.41), it can be seen that the maximum slope efficiency is obtained when all the pump power is absorbed with minimum losses. Hence, if these conditions are satisfied, only the pump wavelength divided by the laser wavelength (λ_p / λ_L) is left in Eq. (1.2.41). This is known as the quantum efficiency and gives the highest possible slope efficiency since in this case, every pump photon is converted to a laser photon. In realistic laser systems, the actual slope efficiency is lower than the ideal quantum efficiency.

As a result, the maximum slope efficiency of a resonator is obtained when the overall losses are very low and all the pump power is absorbed by the gain medium. The relation which combines the threshold pump power, the slope efficiency and the output power can be written as [9]

$$P_{out} = \eta\left(P_{p-}\left(P_p\right)_{th}\right). \tag{1.2.43}$$

Here, P_p is the pump power, $(P_p)_{th}$ is the threshold pump power, and P_{out} is the output power of the laser.

1.3 Cr^{4+}: forsterite Lasers

In this section, a brief history of chromium doped forsterite lasers, information about the crystal structure of the forsterite host, its physical properties, thermal problems, and some of its applications will be presented.

After the discovery of the ruby laser in 1960, the search for new crystal hosts and ions that have emissions in the near-IR region was started. Lasing from a chromium doped forsterite laser was first reported by Petričević et al. in 1988 [10]. The first Kerr-lens mode-locked operation in a Cr^{4+}: forsterite laser system was later reported by A. Seas et al. in 1991 [11].

The forsterite crystal is a member of the olivine family and its chemical formula is Mg_2SiO_4. In this crystal, magnesium atoms form a single bond with two oxygen atoms from the silicate tetrahedron and the overall structure is orthorhombic [12]. If the forsterite crystal is doped with Cr ions, they replace the Mg^{2+} ions in the lattice.

Crystals which are used to build lasers should have high optical transparency as well as chemical and mechanical robustness. Carefully synthesized Cr^{4+}: forsterite crystals fulfill these requirements and can be used as laser gain media. As described above, usually, host materials are doped with rare earth or transition metal ions. Doping the forsterite host with a transition metal ion leads to the formation of a broad gain band near 1300 nm due to electron-phonon coupling. Electron-phonon coupling is simply due to the interaction of the laser-active electrons with the surrounding vibrating lattice. Laser crystals with broad gain bandwidth are important for generating tunable laser light [13] and also ultrashort optical pulses. The equation which gives the relationship between gain bandwidth ($\Delta\lambda$ or $\Delta\nu$) and pulse duration (τ_p), can be written in the form

$$\Delta\nu\tau_p = 0.315. \tag{1.3.1}$$

The constant 0.315 is for pulses which have a temporal profile of the form sech(t/τ_p). The widths in the wavelength and frequency domain are related through

$$\Delta\lambda = \frac{\Delta\nu c}{\nu^2}, \tag{1.3.2}$$

Equivalently, we can also write this relationship as

$$\Delta\nu = \frac{\Delta\lambda c}{\lambda^2}. \tag{1.3.3}$$

Since

$$\nu = \frac{c}{\lambda}. \tag{1.3.4}$$

In Eqs. (1.3.2), (1.3.3), and (1.3.4), ν is the frequency, λ is the operation wavelength of the laser, and c is the vacuum speed of light. The gain bandwidth for the Cr^{4+}: forsterite crystal is around 80 nm giving Δν ~ 15.6 THz. Therefore, the shortest pulse that can be obtained from a Cr^{4+}: forsterite laser is approximately 20 fs. The shortest pulse that has been obtained to date from a Cr^{4+}: forsterite laser is 14 fs [14].

The upper-state lifetime of the Cr^{4+}: forsterite crystal strongly depends on the temperature due to the phonon assisted non-radiative decay of the upper-state population as discussed in Fig. 1.2.2. This creates a practical problem for the efficiency of the laser. The laser efficiency will decrease as a result of the thermal loading in the crystal, and higher pump sources may not yield high output powers due to thermal loading. To avoid this problem, complex cooling mechanisms can be used (e.g. cryogenic cooling). However, efficient room temperature operation of this type of laser by using only water cooling was obtained by A. Sennaroglu [15]. In addition to that, the highest pulse energy (81 nJ) directly obtained

from a mode-locked Cr^{4+}: forsterite laser operating at room temperature was reported by H. Cankaya et al. [16]. In the present thesis, the highest peak powers generated from a solid-state laser by using a single-walled carbon nanotube saturable absorber and graphene based saturable absorber have been demonstrated. As the gain medium, we used a Cr^{4+}: forsterite crystal for both of the experiments [17].

The operation wavelength of the Cr^{4+}: forsterite crystal is around 1.3 μm, which makes this laser a very suitable light source for biomedical applications. Biological tissues are mainly composed of water. If we look at the absorption spectrum of water [18] for various wavelengths, it is obvious that water is strongly absorbed at wavelengths above 1.4 μm.

In addition to absorption, because of Rayleigh scattering, shorter wavelengths are scattered more than the longer wavelengths. Thus, the operation wavelength (1.3 μm) of the Cr^{4+}: forsterite laser is ideal for biomedical imaging applications requiring deep tissue penetration, such as; multi-photon microscopy and optical coherence tomography [19, 20].

Chapter 2

CONTINUOUS-WAVE and PULSED OPERATIONS of LASERS

2.1 Continuous Wave Operation of Lasers

After the oscillation threshold is reached, lasing starts as discussed in Chapter 1. If a time dependent loss or gain mechanism is not introduced into the laser cavity, continuous wave (CW) operation is obtained. During this regime, the output power of the laser remains constant with time and the operating parameters of the laser such as the threshold pump power and slope efficiency can be calculated by using the equations in Chapter 1.
Both pulsed and CW lasers have physical properties which make them different from other light sources. A brief description about these properties will be given in this section. These characteristic features of lasers are; directionality, monochromaticity, spectral brightness, and coherence.

2.1.1 Directionality of Laser Beams

A directional light source does not spread by a considerable amount as it propagates and maintains its spatial profile. Of course, some amount of spreading always takes place due to diffraction. Well designated lasers can produce directional light beams whose spreading is only limited by diffraction. Usually, spherical end mirrors are used at the laser resonator. With this configuration and provided that minimum beam distortion effects occur inside the gain medium, the output beam has a TEM_{00} profile. As such, the radial distribution of the

beam closely resembles a Gaussian function. Furthermore, for the TEM_{00} beam, the spot size, i.e. the radial distance where the electric field decays to 1 / e of its peak value, is given by [9]

$$W(z) = W_0\sqrt{1 + \left(\frac{z - z_f}{z_0}\right)^2}. \tag{2.1.1}$$

Here, z is the propagation direction and w_0 is the beam waist, z_f is the location of the beam waist, and z_0 is a very important beam parameter called the Rayleigh range. z_0 is given by

$$z_0 = \frac{n\pi w_0^2}{M^2\lambda}. \tag{2.1.2}$$

In Eq. (2.1.2), n is the refractive index of the medium and M^2 is the M-square parameter of the laser beam. Which determines how much a beam deviates from the ideal case of the Gaussian beam for which $M^2 = 1$. As seen from the equation above, Rayleigh range also depends on the wavelength of the source and the beam waist. The smaller the initial beam waist, the larger is the diffractive beam spreading of the beam. Beam spreading also increases as the wavelength of the light increases.

2.1.2 Lasers are Monochromatic Light Sources

If an electromagnetic wave is ideally at a single frequency, it is called monochromatic radiation. Different from other light sources, lasers can produce monochromatic light. However, there exists a fundamental limit for the spectral width ($\Delta\nu_0$) of an atomic transition which determines the ultimate spectral bandwidth of a laser. According to this

limit the radiative decay rate gives the minimum spectral width with the following formula [9]

$$\Delta\nu_0 = \frac{A_{21}}{2\pi}\,. \tag{2.1.3}$$

Typically, special techniques such as frequency stabilization are required to operate lasers with a very narrow spectral bandwidth compared to the center frequency. So far, fractional linewidths $\Delta\nu / \nu$, of less than 10^{-15} have been achieved [21].

2.1.3 Spectral Brightness of Lasers

Brightness of an optical beam per unit spectral bandwidth is called as spectral brightness. The spectral brightness of a light source can be defined as [9]

$$B \equiv \frac{P}{A\Omega\Delta\nu}\ , \tag{2.1.4}$$

where P is the output power of the source, A is the area, and Ω is the solid angle. The area of the beam can be written as

$$A = \pi w_0^2\ , \tag{2.1.5}$$

Figure 2.1.1 shows the beam divergence angle θ, and it is given by

$$\theta = M^2\frac{\lambda}{\pi w_0}. \tag{2.1.6}$$

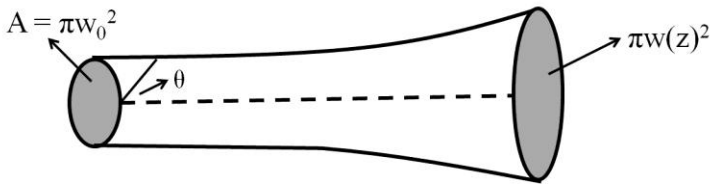

Figure 2.1.1 *Schematic description for the initial Gaussian beam cross-sectional area (adopted from A. Sennaroglu, Photonics and Laser Engineering).*

We can write the solid angle as

$$\Omega = \pi\theta^2 \, . \tag{2.1.7}$$

Since $M^2 = 1$ for the Gaussian beam, the solid angle can be rewritten as

$$\Omega = \frac{\lambda^2}{\pi w_0^2} \cong \lambda^2 \, . \tag{2.1.8}$$

Using Eqs. (2.1.4) and (2.1.8), the spectral brightness at large distances from the beam waist location is:

$$B = \frac{P}{\lambda^2} \, . \tag{2.1.9}$$

Although the output power of an ordinary laser is much lower than other light sources such as the Sun, the narrow spectral bandwidth property gives rise to a high brightness.

2.1.4 Coherence of Laser Beams

A light source produces electromagnetic waves. It is known that, two waves can constructively or destructively interfere. If these waves are perfectly sinusoidal and have a constant phase relative to each other, they are called coherent waves. To examine the temporal coherence of a light source, one can build a Michelson interferometer. Hence, one can measure the intensity of the resulting light which is composed of the electric fields of the two split waves of the same source and find the degree of coherence of a light source.
In reality, no wave source is perfectly coherent and a light source can have a degree of coherence which is determined by the coherence function [9] with the following inequality

$$0 \leq |\gamma_{12}(\tau)| \leq 1. \tag{2.1.10}$$

This coherence function arises from the resulting intensity signal measurement of the Michelson interferometer. If it is equal to one, we have complete coherence. On the other hand, if it is zero, we have complete incoherence. Any other value between one and zero of the coherence function gives partial coherence.
The spectral bandwidth discussed in the previous section gives a certain coherence length for a laser. Fig. 2.1.2 (a) shows the spectral linewidth for a typical laser and Fig. 2.1.2 (b) shows the corresponding sine waves with different periods. For example, consider a nearly coherent light source (i.e. a laser) which consists of a spectral linewidth. Each sine wave will gain a different amount of phase as it propagates over a given distance. Hence, coherence can be stated as

$$\lim_{\frac{\Delta\lambda}{\lambda_0}\to 0} |\gamma_{12}| = 1 \tag{2.1.11}$$

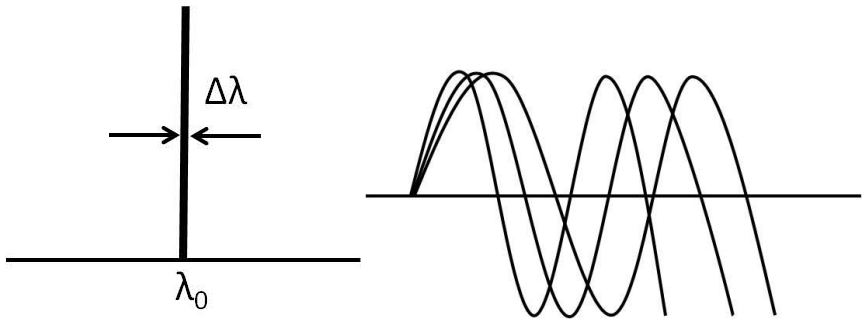

Figure 2.1.2 (a) *A typical spectral linewidth of a laser.* ***(b)*** *Corresponding sine waves with different periods.*

As a result, we can say that even the most coherent light source remains coherent over a certain propagation distance called the coherence length. The coherence length is related to the coherence time through the relation [9]

$$l_c = \tau_c c \ . \tag{2.1.12}$$

On the other hand, lasers also have spatial coherence. The spatial coherence of lasers is related with the phase of each sinusoidal wave at different points located on a plane which is perpendicular to the direction of light propagation. If the spatial coherence is high, the beam profile is not distorted with propagation. As discussed in Section 2.1.1, a laser with high spatial coherence can produce directional light with a pure TEM_{00} profile.

2.2 Pulsed Operation of Lasers

Different from the CW operation, in pulsed regime, the output power of the laser changes with time. If a periodic loss or gain mechanism is introduced into the system, pulsed

operation can be obtained. Depending on the physical mechanism behind the periodic modulation, this operation can be achieved passively or actively. In this section, three main types of pulsed operation will be discussed. These are gain-switched, Q-switched, and mode-locked operations of lasers. However, mode-locked operation will be emphasized, because in our experiments this regime is exploited to produce ultrashort (<1ps) pulses.

2.2.1 Gain-Switched Operation of Lasers

If the optical pump source itself is a pulsed laser, gain-switched operation is obtained. In this case, the pump source directly modulates the optical gain. Since the gain medium of the laser encounters the pump pulses with a short duration, the population inversion in the gain medium is only present for a short time. This results in the production of pulsed output beams from the laser. In this regime, the duration of the output pulses strongly depends on the pulse width of the pump source and they are typically shorter than the pulse duration of the pump source.

2.2.2 Q-Switched Operation of Lasers

Q-switched operation is obtained by changing the Q-factor (quality factor) of the resonator. The Q-factor is a parameter which determines the amount of loss present in the resonator. In order to achieve Q-switched operation, an external (active) or internal (passive) loss mechanism is introduced into the cavity. This component creates loss inside the resonator and lowers the Q-factor. This increases the population in the upper-state energy level of the gain medium. When this mechanism is turned off, the Q-factor of the cavity becomes high again and stimulated emission occurs as a result of transitions from the upper energy level to the lower energy level inside the gain medium. This on and off mechanism occurs in a

very short period of time, which results in the production of short pulses from the laser. In addition to this, due to the large amount of population accumulation in the upper energy level of the gain medium, it is possible to produce pulses with high peak powers. By using this type of operation, depending on the cavity length and the gain medium parameters, pulses with duration in the range of picoseconds to microsecond can be produced.

2.2.3 Mode-Locked Operation of Lasers

Different from the other two techniques, pulse durations much shorter than the cavity round-trip time can be obtained during mode-locked operation. Typical pulse durations are in the picoseconds or femtosecond range.

As a result of the periodic modulation of the circulating laser beam inside the cavity, randomly oscillating modes are locked in phase and pulsed operation is initiated. Similar to the Q-switched regime, this operation can be achieved by using an active or a passive modulator. In this section, mode-locking of the randomly oscillating modes which are supported by the laser cavity will be discussed and then a brief discussion about active mode-locking will be given. The main emphasis will be on the passive mode-locking mechanism. In the following sections, components (e.g. saturable absorbers) which are used to passively modulate the circulating laser beam inside the cavity will be discussed.

The first investigation on the mode-locked operation of lasers was done by Gürs and Müller on ruby lasers [22] and by Statz and Tang on He-Ne lasers [23]. In addition, the first papers which clearly explain the mechanism behind mode-locking operation were written by DiDomenico [24], Hargrove et al. [25], and Yariv in 1964 [26].

Figure 2.2.1 shows a simple resonator with a gain medium and a passive modulator. As a result of the large gain bandwidth, this resonator can support infinitely many longitudinal modes with equally spaced resonant frequencies.

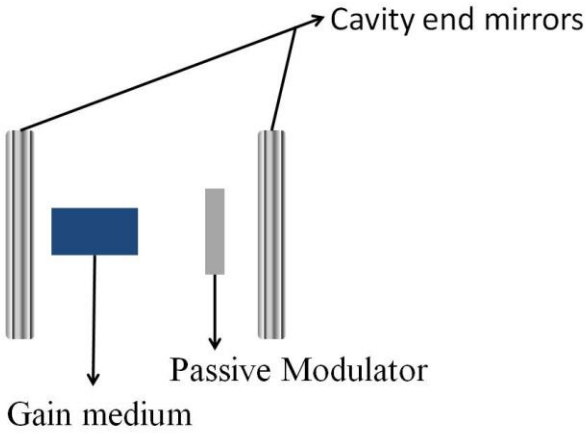

Figure 2.2.1 *Schematic description of a laser resonator with a passive modulator.*

If we take the spatial distribution of the modes as TEM_{00}, these modes will be at discrete frequencies given by

$$\nu_q = q\,\frac{c}{2L_{eff}}\,. \tag{2.2.1}$$

L_{eff} is the effective optical path length of the resonator, and q is an integer number. Furthermore, as seen from Fig. 2.2.2, the frequency spacing between two adjacent modes at discrete frequencies is called the free spectral range given by [9]

$$\nu_{FSR} = \nu_{q+1} - \nu_q = \frac{c}{2L_{eff}}\,. \tag{2.2.2}$$

If these modes simultaneously oscillate in the resonator, the difference between the angular frequencies of the adjacent modes becomes

$$\omega_F = \omega_{q+1} - \omega_q = 2\pi\nu_{FSR} \,. \tag{2.2.3}$$

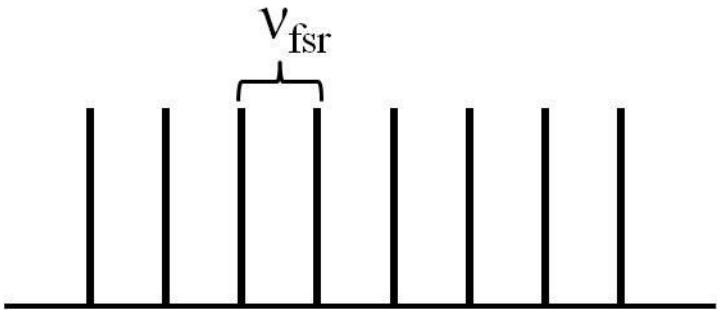

Figure 2.2.2 *Oscillating resonant modes of a laser cavity. Two adjacent modes are separated by one free spectral range.*

If we take the number oscillating modes as M and use the superposition principle, the net electric field due to M locked becomes [9]

$$E(t) = \sum_{q=0}^{M-1} E_q e^{\left(i(\omega_0 + q\omega_F)t + i\varphi_q(t)\right)} \tag{2.2.4}$$

where E_q is the amplitude of the q^{th} mode, ω_0 is the reference angular frequency, and $\varphi_q(t)$ is the phase of the q^{th} mode.

Figure 2.2.3 (a) describes the randomly oscillating modes with such phases. As a result of the random oscillation of each phase, E(t) also varies randomly over time and gives rise to a constant output power with time in the CW regime as described in the first section. Figure 2.2.3 (b) shows that, if these modes are forced to oscillate with the same phase, a periodic train of pulses can be obtained.

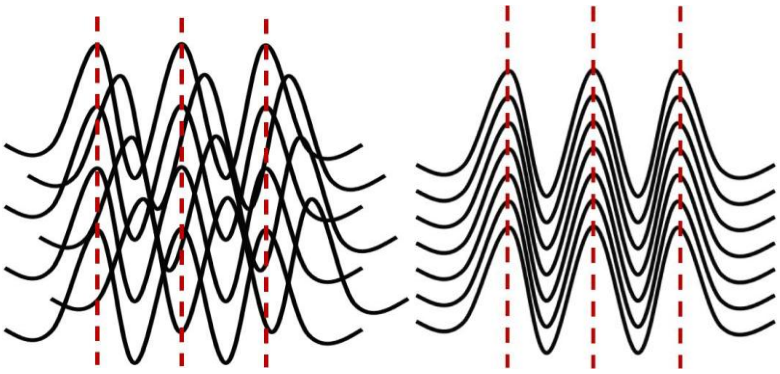

Figure 2.2.3 (a) *Randomly oscillating modes inside the cavity with different phases.* ***(b)*** *Locked modes are oscillating in phase.*

To find the repetition frequency of such pulses, we will continue with the analysis by assuming that the electric field is linearly polarized. If all the phase factors are set to zero in Eq. (2.2.4), and every mode has the same electric field amplitude, then the net electric field can be written as

$$E(t) = E_0 \sum_{q=0}^{M-1} e^{(i(\omega_0 + q\omega_F)t)} \tag{2.2.5}$$

$$= E_0 e^{i\omega_0 t} \frac{1-e^{iM\omega_F t}}{1-e^{i\omega_F t}} \tag{2.2.6}$$

$$= E_0 e^{i\omega_0 t} \frac{\sin\left(\frac{M\omega_F t}{2}\right)}{sin\left(\frac{\omega_F t}{2}\right)}. \tag{2.2.7}$$

Equation (2.2.7) tells us that the electric field has a local maximum at t = 0. The next maximum in the electric field occurs at t = T_R, where T_R and the angular frequency spacing between two modes are related through

$$T_R = \frac{2\pi}{\omega_F} = \frac{2L_{eff}}{c} . \tag{2.2.8}$$

Hence, the periodic pulse train has a repetition frequency (f_{rep}) equal to the free spectral range of the resonator.

$$f_{rep} = \frac{c}{2L_{eff}} . \tag{2.2.9}$$

The pulse width (τ_p) can be defined as the time difference between the peak of the pulse and the first zero, and it can be calculated from [9]

$$\frac{M\omega_F\tau_p}{2} = \pi , \tag{2.2.10}$$

Equivalently, τ_p can be written in terms of T_R as

$$\tau_p = \frac{1}{M}\left(\frac{2\pi}{\omega_F}\right) = \frac{T_R}{M} . \tag{2.2.11}$$

Hence, the duration of pulse is related to the number of locked modes. It can be seen from Eq. (2.2.11) that, if the number of locked modes increases, the pulse width decreases. Also note that T_R / M approximately gives the spectral bandwidth that contains the locked modes of the resonator. Hence we see that

$$\tau_p \approx \frac{1}{\Delta\nu}\,. \tag{2.2.12}$$

If the gain bandwidth for a laser is very large, the number of locked modes will also be very large. For this case, the net electric field of the pulse can be written as a continuous summation in the form

$$E(t) = \int_{-\infty}^{+\infty} d\omega \left[E_p(\omega) e^{i\varphi(\omega)} e^{i\omega t}\right]. \tag{2.2.13}$$

In real laser systems, there are dispersive and nonlinear effects which distort the pulse shape. Details of these effects will be explained in the following chapter. Now, we can say that, if these distortion mechanisms are minimized, the laser can produce pulses as short as allowed by the available gain bandwidth. Such pulses are called transform-limited pulses. For a transform-limited pulse, the product of the temporal duration and the spectral width, usually called the time-bandwidth product can be written as

$$\Delta\nu\tau_p = K\,, \tag{2.2.14}$$

where K is a constant known as the time-bandwidth product. K is equal to 0.315 for pulses with a sech^2 temporal profile and 0.44 for Gaussian pulses.

Now, we are finished with the basic physical principles behind the mode-locking mechanism. We will continue with a brief description of active mode-locking, followed by a detailed discussion of passive mode-locking.

In order to lock the modes in the resonator, an intensity-loss mechanism should be introduced to the overall system. If this loss mechanism modulates the circulating laser beam with the help of an external driver, the technique is called active mode-locking. For

example, an acousto optic modulator, (AOM) which usually consists of a transparent crystal and a piezoelectric transducer to modulate the beam transmission at a given frequency can be used [27]. This loss mechanism acts like a shutter inside the cavity. It opens and closes at a frequency which is equal to the free spectral range of the cavity, and enables the production of a periodic pulse train.

For passive mode-locking of the lasers, this active modulator is replaced with a component commonly known as a saturable absorber. Semiconductor devices such as semiconductor saturable absorber mirrors (SESAMs) can be used as saturable absorbers to obtain mode-locked operation of lasers [28]. Semiconductors consist of a valance and a conduction band, separated by the energy band-gap (E_{gap}). When it is exposed to laser light, a transition occurs from the valance band to the conduction band.

The time required for an excited electron to go back to its original state is called the recovery time of the semiconductor saturable absorber. If this recovery time is shorter than the cavity round-trip time, it is called a fast saturable absorber. Otherwise, it is called a slow saturable absorber. The recovery times of single-walled carbon nanotube and graphene saturable absorbers we used in our experiments are less than 2 ps. Hence, we will continue with the fast saturable absorber analysis in the time domain, given by H. A. Haus [29]. The transmission of the saturable absorber exposed to a time-dependent light intensity I(t) during modulation is given by

$$s(t) = \frac{s_0}{1+\frac{I(t)}{I_{sat}}}. \tag{2.2.15}$$

In the above equation, s_0 is the small-signal loss, I(t) is the time dependent intensity, and I_{sat} is the saturation intensity for the saturable absorber. In the following analysis, s_0 will be smaller than one. For weak saturation, Eq. (2.2.15) can be written as

$$s(t) = s_0 - \frac{s_0 I(t)}{I_{sat}}. \quad (2.2.16)$$

The beam amplitude is normalized such that ($|a(t)|^2$) gives the beam power. Since the beam intensity is defined as the power per unit area, Eq. (2.2.16) becomes

$$s(t) = s_0 - \frac{s_0 |a(t)|^2}{I_{sat} A} \equiv s_0 - \gamma_{sam} |a(t)|^2. \quad (2.2.17)$$

The self-amplitude modulation (SAM) constant (γ) adds a non-linear phase delay to the temporal profile of the pulses. Details of SAM (Self-phase modulation (SPM)) will be given in Chapter 3, and it is defined in Eq. (3.1.10). Now, it will be treated as a constant in the fast saturable absorber analysis. By using the saturation term and omitting the active modulation term, the solution for the master equation of mode-locking given by H.A.Haus [29] will have a sech temporal profile.

Thus, the intensity of light is important for passive mode-locking. If the parameters of the saturable absorber (e.g. saturation intensity, small-signal loss) are optimized, the transmission of the saturable absorber will increase with increasing light intensity. As a result, the oscillation of high intensity light pulses will be favored.

2.3 Semiconductor Based Saturable Absorbers

In this section, three different semiconductor materials used as saturable absorbers for passive mode-locking will be described. These include semiconductor saturable absorber mirrors (SESAMs), single-walled carbon nanotube saturable absorbers (SWCNT-SAs), and graphene based saturable absorbers.

2.3.1 Semiconductor Saturable Absorber Mirrors (SESAMs)

A typical SESAM consists of a highly reflective Bragg mirror structure and a quantum well absorber layer for saturable absorption process [28] Figure 2.3.1 shows the structure of the SESAM. Usually low-temperature grown III-V group semiconductors are used as saturable absorbers and the thickness of the energy band-gaps of the semiconductor based quantum well layer are controlled by a band-gap engineering process to adjust the operation wavelength of the SESAM.

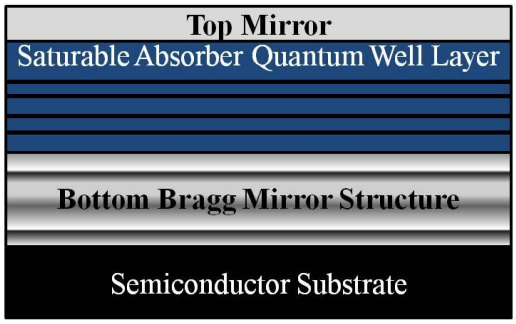

Figure 2.3.1 *Schematic description for a semiconductor saturable absorber mirror (SESAM).*

There are three main design parameters for saturable absorbers. These are the saturation fluence (E_{sat}), recovery time, and non-saturable losses. As discussed above, according to the recovery time of the saturable absorber, it can be classified as a fast or a slow saturable absorber. The recovery time is very important to have efficient mode-locked operation, because when the recovery time is larger than the cavity round-trip time, the laser will have a tendency to operate in the CW or Q-switched regime. Typical carrier life-times in the semiconductors used for SESAMs are in the ns time scale. Hence, they are not suitable for

mode-locking operation. In order to reduce the effective absorption recovery rate of bulk semiconductors, defects are inserted into the structure [30].

The saturation fluence determines how much intensity is needed to saturate the saturable absorber. The mode-locking build up time decreases with small saturation intensities. However, if the saturation intensity is too small, the laser will start to operate in the Q-switched regime. In addition to this, the saturation intensity limits the mode-locking operation with high pulse energies. If the saturable absorber is saturated with intensity much higher than the saturation intensity, multi-pulsed operation may result. The non-saturable losses are not included in the saturation process since they introduce losses to the laser cavity at all intensities. The non-saturable losses can be reduced with low growth temperature. However, the reduced growth temperature will limit the maximum thickness of the absorber material which will be deposited on the SESAM structure.

Hence, the process used to produce high quality SESAMs is very complex and requires expensive facilities to adjust the operation wavelength of the SESAM (e.g. clean rooms). Recently emerging alternatives are single-walled carbon nanotube (SWCNT-SAs) and graphene saturable absorbers (graphene-SAs). Optical characteristics of these materials will be discussed in the following sections.

2.3.2 Graphene Based Saturable Absorbers (Graphene-SAs)

Graphene is a single atomic layer of carbon in the form of honeycomb lattice structure (Fig. 2.3.2). Graphene is a zero gap semiconductor which makes it different from other semiconductor materials. The Nobel Prize in Physics for 2010 was given to Andre Geim and Konstantin Novoselov for their discovery of graphene.

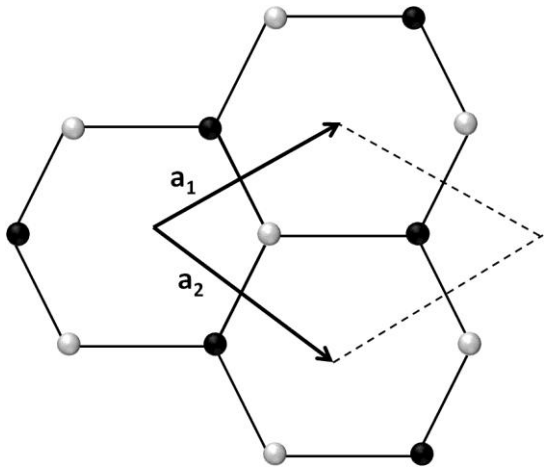

Figure 2.3.2 *Hexagonal lattice structure of graphene with two atoms in the unit cell.* $\boldsymbol{a_1}$ *and* $\boldsymbol{a_2}$ *are the unit cell vectors with lattice constant 2.46 Å.*

Electrons propagating through the graphene have a linear dispersion relation given as [ref]

$$E = h\nu_F|\boldsymbol{k}| \tag{2.3.1}$$

where k is the two dimensional wave-vector and ν_F is the Fermi velocity on the order of 10^6 ms^{-1} [31, 32]. This linear dispersion relation makes broadband applications possible. Graphene also has unique optical properties. Despite being only a monolayer thick, it is optically visual. Graphene reflects the small amount (<0.1 %) of incident light in the visible region. The transmittance (T) of graphene can be expressed in terms of the fine structure constant (α) in the following way [33, 34]

$$T = (1 + 0.5\pi\alpha)^{-2} \approx 1 - \pi\alpha \approx 97.7\%\,, \tag{2.3.2}$$

$$\alpha = \frac{e^2}{4\pi\varepsilon_0 \hbar c} \cong {}^{1}/_{137} \,. \tag{2.3.3}$$

In addition, the optical absorption (A) of graphene layers is proportional to the number of layers. Each layer has a broad absorption over the visible spectrum given by

$$A = 1 - T \approx \pi\alpha \approx 2.3\% \,. \tag{2.3.4}$$

Due to its zero gap structure, the absorption spectrum of the graphene is quite flat from 300 nm to 2500 nm, and a peak around the UV region can be seen due to the exciton-shifted Van Hove singularity in the graphene density of states [35]. The transmission spectrum of graphene that we used in our experiments is given in Chapter 4.

The saturable absorption in graphene is observed due to the Pauli blocking principle. If the incident light intensity is strong enough, the generated carriers will fill the entire valance band and do not allow any excitation. Hence, the photons will be transmitted without a loss. During the excitation process, an electron-hole pair in resonance to that excitation will be produced. Since the recovery time of this electron-hole pair is fast for graphene based saturable absorbers (<2ps), graphene can provide passive mode-locking operation for lasers. In addition to this, because of its zero band gap structure, in practice regardless of the wavelength, the same saturable absorber can be used for lasers operating over a wide range of wavelengths.

2.3.3 Single-Walled Carbon Nanotube Saturable Absorbers (SWCNT-SAs)

Carbon-nanotube structures are formed by rolled-up single atomic sheets of carbon (graphene). These nanotube structures are discovered by Sumio Iijima in 1991 [36]. There

are different types of carbon nanotubes depending on their combination of the rolling angle and radius. There is pair of indices (n,m) which determines the metallic or semiconductor character of the carbon nanotubes [37]. These two integers denote the number of unit vectors along the corresponding directions in the honeycomb lattice of graphene. If m is equal to zero, we have zig-zag type carbon nanotubes. For m equal to n, we have armchair-type nanotubes. Otherwise, the structure is called a chiral type nanotube. Figure 2.3.3 shows the schematic structure for the different types of carbon nanotubes. There are also multi-walled nanotubes, which can be described as concentric tubes.

Carbon nanotubes are promising candidates for many applications. They are robust materials and they have favorable characteristics for optical as well as electronic applications. They are particularly interesting for photonic applications because of their direct band-gap structure and high third order susceptibility [38].

Singe-walled carbon nanotube saturable absorbers (SWCNT-SAs) are used for passive mode-locking of lasers because of their fast recovery time (<2ps). The saturation and

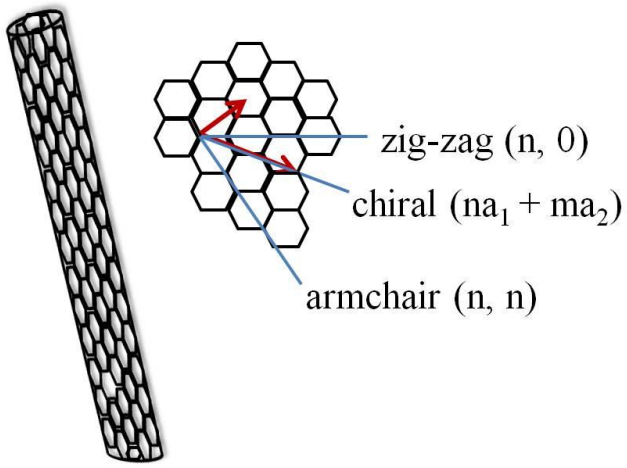

Figure 2.3.3 *Carbon nanotube is a rolled-up graphene sheet. This rolling angle with unit cell vectors and n, m indices determine the structure, and diameter of carbon nanotube.*

mode-locking mechanism is similar to what was described above for SESAMs. Different from SESAMs, they can be used for a variety of wavelengths, depending on the nanotube diameter which determines the operation wavelength. The diameters of carbon nanotubes are usually around 1-3 nm, which makes them good saturable absorbers for near-IR lasers. In addition to these properties, SWCNT-SAs do not require complex and expensive fabrication techniques like SESAMs. Hence, they are becoming a quite attractive alternative for the passive mode-locking of laser systems.

As a result, regardless of the operation wavelength, the majority of the lasers need saturable absorber materials in order to obtain mode-locked operation. Currently, the most common technology is SESAM. However, graphene-SAs and SWCNT-SAs can be alternatives for this technology. SESAMs suffer from narrow operation range and complex fabrication techniques. SWCNT and graphene are cost-effective materials and do not require complex fabrication techniques. In addition, by controlling the diameter distribution of the SWCNT, they can be utilized in various wavelength ranges, especially in the near-IR range [39]. Furthermore, graphene is superior to any other semiconductor saturable absorber in terms of covering the electromagnetic spectrum. Since it has zero band gap structure and nearly the same absorption in the 300-2500 nm range, the same graphene saturable absorber can be used to passively mode-locked many different types of lasers [39].

Chapter 3

THIRD-ORDER OPTICAL NONLINEARITIES and MULTI-PASS CAVITIES (MPCs)

In this part of the thesis, third-order nonlinear optics and multi-pass cavities will be presented. Chapter 3.1 discusses dispersion, electromagnetic wave propagation in dispersive medium, self-phase modulation, nonlinear refractive index, and solitary pulses. Then, brief information about dispersion controlling optics (e.g. Gires-Tournois Interferometer (GTI), chirped mirrors) used in our experiments will be given. In the second part of this chapter, introductory discussion about the ABCD matrix formalism and the complex q-parameter of a laser will be presented. The last part of Chapter 3.2 discusses multi-pass cavities (MPCs), and the MPC design used in our experiments.

3.1 Nonlinear Optics

Nonlinear optics is a huge branch which encompasses lots of different optical phenomena. Ultrafast optics and nonlinear optics are mainly based on the propagation of light in a material medium. For lasers, the intensity of light which passes through the medium can be sufficiently high to observe nonlinear effects. As a result, the induced polarization in medium has nonlinear components, as well as a linear part. The linear part is responsible for classical optical effects such as reflection and refraction. On the other hand, according to the degree of the nonlinearity, second harmonic generation, third harmonic generation,

Kerr effect, Raman effect are the results of the second and the third-order nonlinear parts of the induced polarization in a medium.

In this chapter, we will discuss third-order nonlinear optics, because it is important to understand the pulse shaping mechanisms behind the solitary pulses, to interpret our experimental results and to have a reasonable understanding of ultrafast optics.

3.1.1 Pulse Propagation in Dispersive Media

In dispersive media, the susceptibility, refractive index, and speed of light are frequency dependent. As a result of the frequency dependent speed of light in a medium, each of the frequency components experience different time delays and the width of the pulse broadens in time (Fig. 3.1.1). If we denote a(z,t) as the pulse envelope function and $|a(z,t)|^2$ as the instantaneous power, the evolution of the pulse envelope function in the presence of different orders of dispersion becomes [9]

$$\frac{\partial a}{\partial z} = \frac{a(z+dz,t)-a(z,t)}{dz} = \sum_{m=1}^{\infty} \frac{(-i)^{m+1}}{m!} k_m \frac{\partial^m a}{\partial t^m}. \tag{3.1.1}$$

The effect of dispersion on pulses is due to the group delay dispersion (GDD) parameter of the medium. The GDD parameter (D) is defined as [9]

$$D = \frac{d^2\phi}{d\omega^2} = l\frac{d^2k}{d\omega^2} = lk_2 = l\frac{d}{d\omega}\frac{1}{u_g} = \frac{d}{d\omega}\left(\frac{l}{u_g}\right). \tag{3.1.2}$$

In following figures (Fig. 3.1.1 (a), (b), (c)), the effect of positive and negative dispersion parameter on a Gaussian pulse can be seen. The time (T) is measured in the reference frame which moves at the group velocity of the pulse and is equal to

$$T = t - \frac{z}{u_g}. \tag{3.1.3}$$

for following figures.

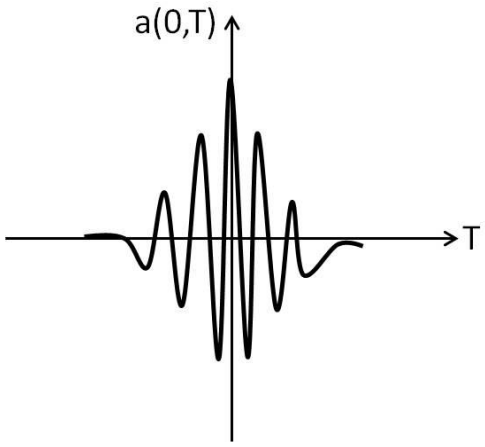

Figure 3.1.1 (a) *Schematic description for the electric field of an incident Gaussian pulse.*

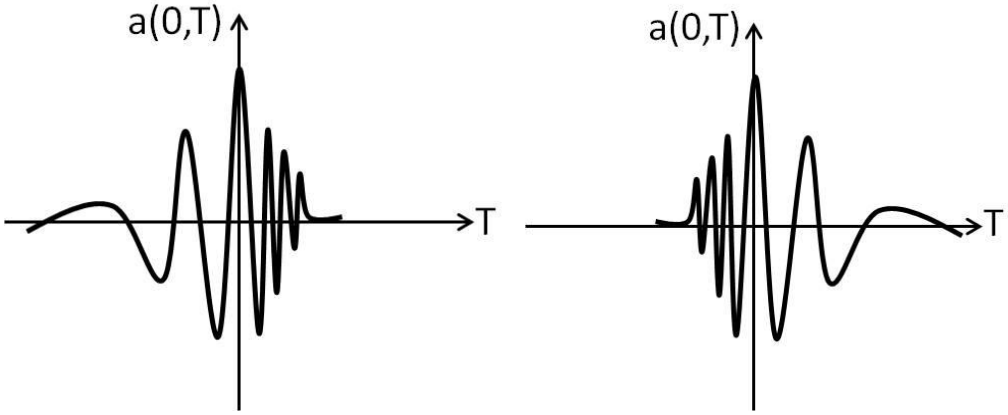

Figure 3.1.1 (b).*Schematic description for the case where D>0, and* ***(c)*** *for the case where D<0 (adopted from A. Sennaroglu, Photonics and Laser Engineering).*

The second-order dispersion adds chirp to the pulse and broadens its temporal profile. For (D > 0), the dynamic frequency is downshifted at the leading edge and vice versa for (D < 0).

In Eq. (3.1.2), ϕ is the phase acquired by the pulse, ω is the angular frequency, l is the length of the medium, and u_g is the group velocity which can be defined as

$$u_g = \frac{d\omega}{dk} \tag{3.1.4}$$

Here, k is the wave vector which is a function of frequency for dispersive media, and for linearly polarized electric field, it can be expanded in a Taylor series about ($\omega = \omega_0$) the central carrier frequency (ω_0) [9]:

$$k(\omega) = k_0 + \left(\frac{dk}{d\omega}\right)_0 (\omega - \omega_0) + \frac{1}{2}\left(\frac{d^2k}{d\omega^2}\right)_0 (\omega - \omega_0)^2 + \cdots \tag{3.1.5}$$

Therefore, in Eq. (3.1.2), l / u_g gives the group delay, and k_2 equals

$$k_2 = \left(\frac{d^2k}{d\omega^2}\right)_{\omega=\omega_o}. \tag{3.1.6}$$

Hence, D is the group delay dispersion parameter and leads to temporal broadening for the light passing through the medium. D is defined in Eq. (3.1.2) in the standard convention of ultrafast optics, and the unit of D is fs^2. Another equivalent definition of D contains the wavelength dependence of the refractive index of medium (n) according to

$$D = l\frac{\lambda^3}{2\pi c^2}\frac{d^2n}{d\lambda^2}. \tag{3.1.7}$$

3.1.2 Nonlinear Refractive Index and Self-Phase Modulation

The nonlinear refractive index is the intensity-dependent contribution to the refractive index of a medium. With this contribution, the refractive index varies according to

$$n = n_0 + n_2 I. \tag{3.1.8}$$

In Eq. (3.1.8), n_0 is the low intensity refractive index, I is intensity of the laser beam, and n_2 is the nonlinear refractive index. Positive nonlinear refractive index of the medium leads to self-focusing of the beam. The laser beam typically has a Gaussian profile and its intensity is higher at the center of the beam. As a result, the induced change in the refractive index will be maximum at the center of the beam. Therefore, the medium will act as a positive lens and focus the beam. In every pass through the medium, the beam will be more focused until the beam eventually collapses. Self-focusing becomes strong when the beam power goes above the so called critical power, which is given by [40].

$$P_{cr} = \frac{\alpha \lambda^2}{8\pi n_0 n_2} \tag{3.1.9}$$

where α is a dimensionless correction factor of the order of unity. If the nonlinear refractive index of the medium is known, the critical power can be calculated easily. Right at the critical power, the beam ideally propagates without undergoing diffractive spreading. At higher power levels, the beam collapses. In a laser operating in the solitary regime, the critical power roughly gives an upper limit to the peak power that can be obtained during single-pulse mode-locked operation.

This nonlinear polarization generation in a medium is known as the Kerr effect. Self-focusing of the beam is a result of the Kerr effect and may be advantageous for some cases. For example, lasers can be operated in the mode-locked regime by exploiting Kerr-induced self-focusing. This is known as Kerr lens mode-locking (KLM) [41].

Kerr nonlinearities also lead to self-phase modulation of the pulse. Since the laser pulse is sufficiently intense to induce a change in the refractive index, it will create a time-dependent refractive index in the medium which will cause a phase variation across the pulse.

If the second-order dispersion is not included, the evolution of the pulse envelope due to Kerr effect can be written as [9]

$$\frac{\partial a}{\partial z} = -i\gamma a(z,T)|a(z,T)|^2 \tag{3.1.10}$$

Here, T is as defined in Eq. (3.1.3), and γ is the Kerr nonlinearity coefficient given by

$$\gamma = \frac{2\pi}{\lambda}\frac{n_2}{A_{eff}}. \tag{3.1.11}$$

Above, A_{eff} is the effective area of the beam. If the nonlinear refractive index of the medium is known, the soliton-area theorem can be used to relate the pulse energy to the pulse width for a given amount of dispersion (D) and Kerr nonlinearity. From this theorem, one can determine the amount of dispersion needed to compensate the self-phase modulation and to have solitary optical pulses. The soliton-area theorem can be expressed as [29]

$$W\tau = \frac{4|D|}{\gamma} \tag{3.1.12}$$

W is the intracavity pulse energy and τ is the pulse width. Both of them can be determined from the experimental data. The properties of solitary pulses will be presented in detail in the following section. Now, we will discuss how the self-phase modulation shapes the temporal profile of the pulse.

If we assume that the power ($|a(z,T)|^2$) remains nearly constant and has an initial value P(0,T), the pulse envelope function over short distances becomes

$$a(z,T) \cong a(0,T)e^{(-i\gamma P(0,T)z)} \tag{3.1.13}$$

and the nonlinear phase shift equals

$$\phi_{NL}(z,T) = -\gamma P(0,T)z. \tag{3.1.14}$$

Let us consider a Gaussian pulse as an input with the envelope

$$a(z,T) = a_0 e^{-\alpha T^2} \tag{3.1.15}$$

where a_0 is a constant. The peak power (P_0) of the pulse equals to magnitude squared of this constant. The nonlinear phase shift can be written as [9]

$$\phi_{NL}(z,T) = -\phi_{max} e^{-2\alpha T^2} \tag{3.1.16}$$

where the maximum nonlinear phase shift is given by

$$\phi_{max} = \gamma z |a_0|^2. \tag{3.1.17}$$

3.1.3 Solitary Optical Pulses

Self-phase modulation imposes a phase shift on the pulse envelope during propagation. This can counteract pulse broadening in time domain. Equation (3.1.12) clearly shows that, the width of the pulse is proportional to the amount of negative dispersion. Self-phase modulation acts as positive dispersion, and to overcome pulse spreading, negative dispersion is needed. Figure 3.1.2 shows that this combination cancels the frequency chirp, and pulse maintains its shape with minimum distortion.

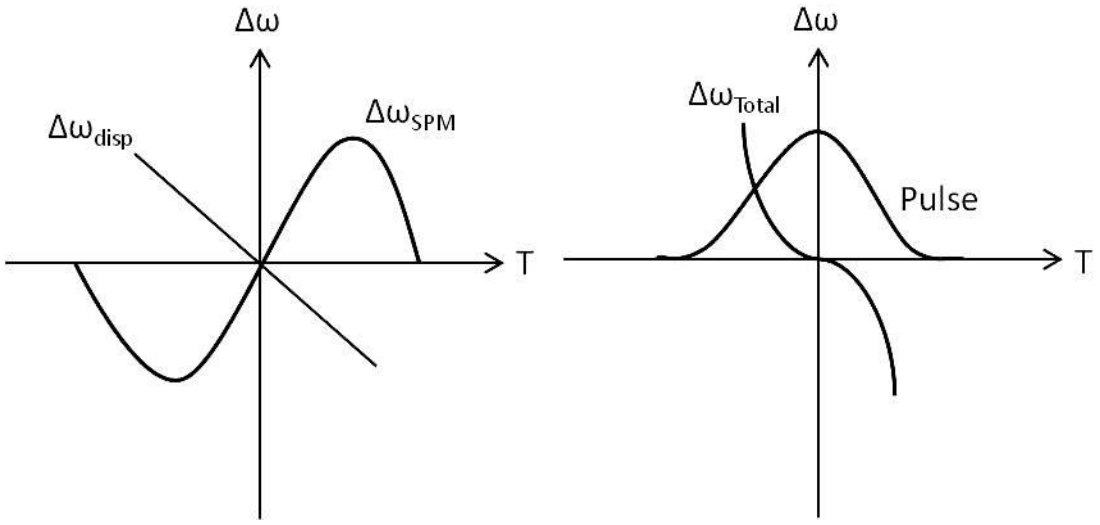

Figure 3.1.2 (a) *Self-phase modulation and negative second-order dispersion curves.* ***(b)*** *Combination of the self-phase modulation and second-order negative dispersion cancels each other which leads to generation of solitary pulses (adopted from A. Sennaroglu, Photonics and Laser Engineering).*

To understand the mechanism behind this cancellation, we can outline a solution to the evolution of the pulse envelope in the presence of both the second-order dispersion and the Kerr effect. The evolution of the pulse envelope can be written as [9]

$$\frac{\partial a}{\partial z} - i\frac{k_2}{2}\frac{\partial^2 a}{\partial T^2} + i\gamma a(z,T)|a(z,T)|^2. \tag{3.1.18}$$

By using the transformations given in [9], we can express the parameters appearing in Eq. (3.1.18) in dimensionless form as

$$\tau = \frac{T}{\tau_0}, \tag{3.1.19}$$

$$x = \frac{|k_2|}{\tau_0^2} z, \tag{3.1.20}$$

$$\psi = \tau_0 \sqrt{\frac{\gamma}{|k_2|}}\, a. \tag{3.1.21}$$

Equation (3.1.18) in its dimensionless form then becomes

$$-i\frac{\partial \psi}{\partial x} - \frac{sgn(k_2)}{2}\frac{\partial^2 \psi}{\partial \tau^2} + \psi|\psi|^2 = 0 \tag{3.1.22}$$

where sgn is the signum function defined according to

$$sgn(k_2) = \begin{cases} 1, & k_2 > 0 \\ -1, & k_2 < 0 \end{cases} \tag{3.1.23}$$

If we consider the case $k_2 < 0$ Eq. (3.1.18) becomes

$$-i\frac{\partial\psi}{\partial x}+\frac{1}{2}\frac{\partial^2\psi}{\partial\tau^2}+\psi|\psi|^2=0. \tag{3.1.24}$$

This equation is called the nonlinear Schrödinger equation. The fundamental soliton solution of Eq. (3.1.24) can be written in analytical form as [9]

$$\psi(x,\tau)=\operatorname{sech}(\tau)\,e^{\frac{ix}{2}}. \tag{3.1.25}$$

Therefore, if the effect of the self-phase modulation is cancelled by negative dispersion, a solitary optical pulse can be obtained with the sech-shaped temporal profile. The pulse duration ($_{T1/2}$, FWHM(full-width half maximum)) for this kind of temporal profile is equal to $1.76T_0$, and the peak power of the fundamental soliton without any distortion equals

$$P_1=\frac{3.11|k_2|}{\gamma T_{1/2}^2}. \tag{3.1.26}$$

To obtain higher-order soliton solutions (i.e. N^{th} order) of Eq. (3.1.24) one can use the input pulse with a form

$$\psi(0,T)=Nsech(\tau) \tag{3.1.27}$$

3.1.4 Gires-Tournois Interferometer and Chirped Mirrors

By introducing negative dispersion to the laser cavity, one can compensate the effect of self-phase modulation and obtain solitary pulses as described in the preceding section. There are different optical components which can give negative dispersion. For example, prism pairs and gratings have been widely used to control the dispersion inside a resonator. In addition, specially designed mirrors can be used to give negative dispersion to the laser cavity. In our experiments, to control the dispersion and to compensate the pulse spreading effect coming from the nonlinearity of the forsterite crystal, we used Gires-Tournois interferometer mirrors (GTIs) and double chirped mirrors (DCMs). Therefore, the characteristics of these mirrors will be presented in this section.

GTI mirrors were introduced by Gires-Tournois et al. [42] as an alternative approach for pulse shaping. GTI is similar to a Fabry-Pérot interferometer but one of the mirrors (M_2) is almost perfectly reflective. Because of this perfect reflection, this device practically does not change the energy of the pulse while tuning its phase. The schematic description for a GTI mirror can be seen in Fig. 3.1.3. Since different frequency components of the pulse propagate different distances in this mirror coating, broadened parts of the pulse are compensated by bouncing the beam from GTI mirrors. The negative dispersion coming from the GTI mirror can be adjusted by changing the mirror separation or changing the angle of incidence in Fig. 3.1.3

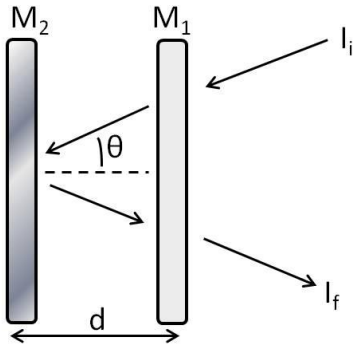

Figure 3.1.3 *Gires-Tournois interferometer is similar to a Fabry-Pérot interferometer.I_i, and I_f are the initial and final intensities, respectively. d is the separation between mirrors, and θ is the angle of incidence.*

However, for femtosecond pulses, the mirror spacing should be of the order of microns which is not practical. This problem was solved by Happner and Kuhl [43] by introducing a different kind of GTI mirror design. This design is based on multilayer dielectric coatings (Fig. 3.1.4).

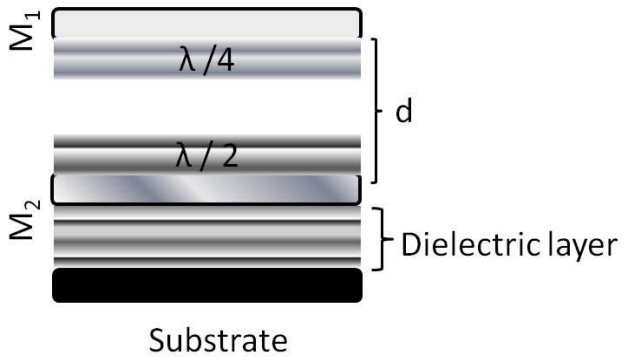

Figure 3.1.4 *Description for the GTI mirror design introduced by Happner and Kuhl (adopted from J. C. Diels, and W. Rudolph, Ultrashort Laser Pulse Phenomena).*

The perfect reflector (M_2) is a sequence of dielectric coatings with alternating refractive indices. These coatings are deposited on a substrate. The spacing d consists of a series of $\lambda / 2$ materials. The other partially reflective mirror consists of a $\lambda / 4$ material layer with high refractive index. With this GTI mirror design, the negative dispersion of the mirror can be easily controlled for femtosecond pulses.

Another alternative is to use chirped mirrors. Chirped mirrors are similar to GTI mirrors but they are formed by depositing dielectric multilayer film sequences with certain refractive index and thickness on transparent substrates. For most of the experiments, a constant reflectivity and a constant amount of dispersion are preferred over the wavelength range of interest. Szipocs et al. [44] first introduced the concept of chirped mirrors. According to their design, chirped mirrors are composed of alternating high and low refractive index materials with varying thicknesses. Therefore, similar to GTI mirrors, different frequencies are reflected at different depths as seen in Fig. 3.1.5. Nevertheless, because of the first air-film interface, undesired sub-resonances occur in the chirped mirrors. Double chirped mirrors (DCMs) introduced by Kaertner et al. [45] are the optimized version of chirped mirrors. By optimizing the modulation ratio of the high and low refractive index layers, chirped mirrors with reduced dispersion oscillation can be achieved.

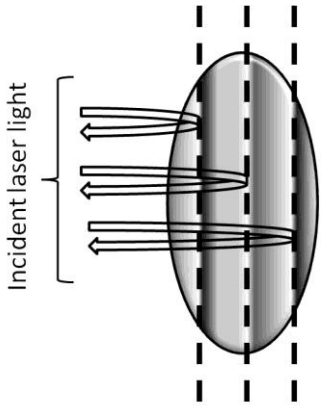

Figure 3.1.5 *Chirped mirrors are composed of dielectric films with alternating refractive indices. Different frequency components of the incident laser light travel different distances in the coating of the chirped mirror, hence acquiring a negative dispersion (adopted from J. C. Diels, and W. Rudolph, Ultrashort Laser Pulse Phenomena).*

3.2 Multi-Pass Cavities (MPCs)

Most of the scientific applications require high pulse energies from compact and cost-effective laser resonators. To have high pulse energies, regenerative amplification techniques have been used [46]. However, cavity extension is a cost-effective alternative to achieve high pulse energies with low pump powers. The pulse energy of a laser can be calculated by dividing its average output power by its repetition rate. As described in Eq. (2.2.9), the repetition rate of a pulse is decreased by increasing the effective cavity length. Therefore, to achieve higher pulse energies with the same average output power, the pulse repetition rate should be reduced. Multi-pass cavity extensions (MPCs) enable high pulse energy generation directly from a laser in a compact and cost-effective way. In MPC, the laser beam undergoes multiple reflections before returning back to the original short cavity. If the beam completes n round-trips in the MPC and the separation between MPC mirrors is

d, the effective optical length of this extension becomes 2nd. In order to preserve the beam parameters (q-parameter) and the average output power of the short cavity, the MPC design should be made with careful analysis. To gain insight about laser resonator stability and q-preserving operation of MPC, basics of ABCD matrix formalism for MPC design and q-parameter of the laser beam will be presented.

3.2.1 ABCD Matrix Formalism

An optical system can be described as a black box which modifies the initial ray parameters. If we do not consider the wave aspects of light and assume that the laser light consists of rays, we can use geometrical optics to understand how this black box operates and modifies an incident ray of light. Mirrors and lenses with different radii of curvatures are used in laser resonators. In addition to this, an incident ray passes through different media with different refractive indices and lengths. All of these optical components are the building blocks of an optical system. If all of these components are located at an optical axis z, the input and output planes of this optical system are located at $z = z_i$ and $z = z_o$, respectively. Two parameters can be used to define a light ray: its height (**r**) and its slope (θ) made with the optical axis. Hence, it can be described as 2x1 column vector

$$\boldsymbol{r} = \begin{bmatrix} r \\ \theta \end{bmatrix}. \tag{3.2.1}$$

This ray enters an optical system with an initial height and slope and leaves with a different final height and slope as can be described by the following column vectors:

$$\boldsymbol{r_i} = \begin{bmatrix} r_i \\ \theta_i \end{bmatrix} \tag{3.2.2}$$

and

$$\boldsymbol{r_f} = \begin{bmatrix} r_f \\ \theta_f \end{bmatrix}. \tag{3.2.3}$$

Therefore, the optical system modifies the ray through the following relation

$$\boldsymbol{r_f} = \boldsymbol{M_T r_i} \tag{3.2.4}$$

where

$$\boldsymbol{M_T} = \begin{bmatrix} A & B \\ C & D \end{bmatrix} \tag{3.2.5}$$

is the ray transfer matrix. Two special input rays can be used to determine the elements of this transfer matrix. The first ray is $\boldsymbol{\rho_1}$ with finite initial height (r_0) and zero initial slope. The second ray is $\boldsymbol{\rho_2}$ with finite initial angle (θ_0) and zero initial slope. Equation (3.2.4) can be written in an open form as

$$r_f = Ar_i + B\theta_i \tag{3.2.6}$$

and

$$\theta_f = Cr_i + D\theta_i. \tag{3.2.7}$$

If we use the conditions for the first ray and the second ray, the elements of the transfer matrix become

$$A = \frac{r_{f1}}{r_0} \tag{3.2.8}$$

$$B = \frac{r_{f2}}{\theta_0} \tag{3.2.9}$$

$$C = \frac{\theta_{f1}}{r_0} \tag{3.2.10}$$

$$D = \frac{\theta_{f2}}{\theta_0} \tag{3.2.11}$$

There are three important rules for the ABCD matrix formalism [9]:

1) The overall ray transfer matrix for a cascaded optical system can be written as

$$\boldsymbol{M_T = M_{T_n} M_{T_{n-1}} \dots M_{T_1}} = \prod_{i=n}^{1} \boldsymbol{M_{T_i}} \tag{3.2.12}$$

2) To have a stable resonator, the following inequality should be satisfied

$$\left|\frac{A+D}{2}\right| \leq 1 \tag{3.2.13}$$

This inequality guarantees that the ray height is bounded and the laser resonator is stable. For equality, the resonator is conditionally stable, which means that a slight misalignment of mirrors will cause the ray to leave the cavity.

3) Any paraxial optical system can be described as the composition of displacements and a thin lens. Transfer matrices for the displacement d and the thin lens with a focal length f can be written as

$$\boldsymbol{M_{T_d}} = \begin{bmatrix} 1 & d \\ 0 & 1 \end{bmatrix} \tag{3.2.14}$$

$$\boldsymbol{M_{T_l}} = \begin{bmatrix} 1 & 0 \\ -\frac{1}{f} & 1 \end{bmatrix} \tag{3.2.15}$$

3.2.2 The Gaussian q-Parameter

This q-parameter for the Gaussian beam gives the radius of curvature and spot size function of the beam. If the complex q-parameter is known, information about radius of curvature and spot size of the beam is also known at a particular location. The complex q-parameter is expressed in the form [9]

$$\frac{1}{q(z)} = \frac{1}{R(z)} - i\frac{\lambda}{n_0 \pi w^2(z)} \tag{3.2.16}$$

In Eq. (3.2.16), R(z) is the radius of curvature and w(z) is the spot size function given in Eq. (2.1.1). The radius of curvature function is given by [9]

$$R(z) = (z - z_f)\left[1 + \left(\frac{z_0}{z - z_f}\right)^2\right]. \tag{3.2.17}$$

Preserving the q-parameter of the laser beam is important for matching modes of the laser beam and the pump beam for KLM (Kerr-lens mode-locking) operation of lasers. To satisfy the q-preserving condition, the initial and final q-parameters of the beam should be equal to each other after n round-trips inside the resonator. If the laser beam returns to its

initial location after n round-trips, the determinant of the transfer matrix should be unity. In other words,

$$AD - BC = 1 \tag{3.2.18}$$

In addition, from Eq. (3.2.13), we can say that the trace of the transfer matrix should remain invariant since we are dealing with a resonator.

After the n^{th} and $(n+1)^{th}$ round-trips, the q-parameter for a self-consistent Gaussian beam should satisfy [9]

$$q_n = q_{n+1} \tag{3.2.19}$$

or

$$q_{n+1} = \frac{Aq_n + B}{Cq_n + D}\,. \tag{3.2.20}$$

Therefore, the q-parameter of the beam also satisfies the following relation at any particular position

$$q = \frac{Aq + B}{Cq + D} \tag{3.2.21}$$

Eq. (3.2.21) can be written as

$$Cq^2 + Dq - Aq - B = 0. \tag{3.2.22}$$

By using Eq. (3.2.18), and solving for 1 / q, we obtain

$$\frac{1}{q} = \frac{D-A}{2B} \pm i\frac{\sqrt{1-\left(\frac{A+D}{2}\right)^2}}{B} \tag{3.2.23}$$

Here, only the negative imaginary part gives a confined Gaussian beam, if we compare with Eq. (3.2.16). Therefore, the radius and spot size of the self-consistent Gaussian beam become

$$\frac{1}{R} = \frac{D-A}{2B} \tag{3.2.24}$$

and

$$\frac{\lambda}{n_0 \pi w^2} = \frac{\sqrt{1-\left(\frac{A+D}{2}\right)^2}}{B}. \tag{3.2.25}$$

3.2.3 MPC Design Rules

The MPC concept was first introduced by Herriot et al. [47]. They have been used for cavity extension in many laser systems [48]. In its simplest form, the MPC consists of two highly reflecting mirrors and notches for beam injection and extraction. Figure 3.2.1 shows a possible MPC configuration with two mirrors and notches. In an ideal case, the MPC should be q-preserving and stable. However, there are also MPC designs which do not satisfy the q-preserving condition or stability condition described in Eq. (3.2.13) [48]. However, q-preserving MPC design is preferred in our experiments in order not to perturb the mode-matching condition of the short resonator. If the MPC satisfies Eq. (3.2.13), the two eigenvalues of the ray transfer matrix have unit magnitude and can be written as [9]

$$\lambda_{\pm} = e^{\pm i\varphi}. \tag{3.2.26}$$

Here,

$$cos\varphi = \frac{(A+D)}{2} \tag{3.2.27}$$

which means that the resonator is stable, and the ray height is bounded. Hence, the ray transfer matrix for the laser beam that bounces n times inside the MPC can be written as [9]

$$\boldsymbol{M_T^n} = \begin{bmatrix} \frac{A-D}{2}\frac{sinn\varphi}{sin\varphi} + cosn\varphi & B\frac{sinn\varphi}{sin\varphi} \\ C\frac{sinn\varphi}{sin\varphi} & \frac{D-A}{2}\frac{sinn\varphi}{sin\varphi} + cosn\varphi \end{bmatrix}. \tag{3.2.28}$$

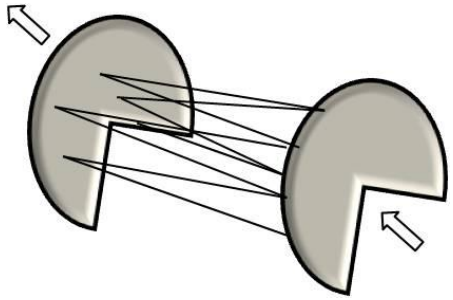

Figure 3.2.1 *Schematic of a multi-pass cavity (MPC). An incident laser light is injected into the cavity from the first notch and after it bounces multiple times, it goes through the second notch.*

If we apply this transfer matrix on an initial ray given in Eq. (3.2.2), after n round-trips the final ray vector becomes

$$\boldsymbol{r_n = M_T^n r_i}. \tag{3.2.29}$$

If we set the initial offset and inclination angle along the x and y directions as (x_0, θ_{x0}), (y_0, θ_{y0}), the final offsets after the n^{th} round-trips become

$$x_n = x_0 cosn\varphi + \left(\frac{x_0(A+D)+2B\theta_{x0}}{2sin\varphi}\right) sinn\varphi \tag{3.2.30}$$

$$y_n = y_0 cosn\varphi + \left(\frac{y_0(A-D)+2B\theta_{y0}}{2sin\varphi}\right) sinn\varphi \tag{3.2.31}$$

which describe an ellipse, and φ stands for the angular advance of the spot pattern after each round-trip. If the initial conditions are set accordingly, one can obtain a circular pattern on the MPC mirrors as well.

As we described before, the q-preserving condition for a laser is important for specific applications. In an ideal case, the MPC should not change the original Gaussian beam parameters, if it satisfies Eq. (3.2.19). Detailed discussion about q-preserving MPCs is given in [48]. However, we can say that, the ray transfer matrix for the MPC should be of the form

$$\boldsymbol{M_T^n} = (-1)^m \boldsymbol{I} \tag{3.2.32}$$

if the angular advance φ = mπ / n, and **I** is the identity matrix given by

$$\boldsymbol{I} = \begin{bmatrix} 1 & 0 \\ 0 & 1 \end{bmatrix}. \tag{3.2.33}$$

Here, m and n are both integers, they stand respectively for the number of round-trips and the number of semicircular paths that the spot pattern on MPC mirrors completes before exciting the MPC. For a flat-curved MPC extension with notches and the radius of curvature of the curved mirror is R_2, to satisfy the q-preserving MPC extension, the separation between the mirrors can be calculated through following relation for specific n and m values [48]

$$d = \frac{R_2}{2}\left(1 - cos\left[\frac{m\pi}{n}\right]\right). \tag{3.2.34}$$

In conclusion, if the effective length of the MPC is 2nd, by combining information coming from Eq. (2.2.9) and Eq. (3.2.34), we can say that, to achieve the desired pulse energy, one should carefully choose integer numbers n and m. In addition, since these integers are related with the angular advance, Eq. (3.2.27) and Eq. (3.2.34) should be considered for a stable and q-preserving MPC design.

Chapter 4

EXPERIMENTAL RESULTS and CONCLUSION

In this final chapter, the experimental set-up of the Cr^{4+}: forsterite laser, fabrication stages for single-walled carbon nanotube saturable absorber (SWCNT-SA), graphene saturable absorber (graphene-SA), and mode-locked operation results will be presented. In the first part, details of the experimental set-up and continuous wave operation of the Cr^{4+}: forsterite laser will be presented. In the second and the third parts, fabrication details and mode-locked operation results with SWCNT-SA and graphene-SA will be discussed. Summary of all experiments and their analysis will be given in Chapter 5.

4.1 Experimental Set-Up and Continuous Wave (CW) operation of the Cr^{4+}: forsterite laser

Initially, the short x-cavity was constructed with two curved dispersion compensation mirrors (DCMs), each with 10 cm radius of curvature (RC). A continuous-wave Yb:fiber laser operating at 1064 nm was used for end-pumping the crystal. A 20 mm long, Brewtser-cut Cr^{4+}: forsterite crystal with 70 % absorption at the pump wavelength was used during the experiments. The crystal was placed between M1 and M2, and the pump beam was focused to an estimated 30 μm waist inside the crystal by using a lens (L1) with 20 cm focal length. The Cr^{4+}: forsterite crystal was mounted in a copped holder and maintained at a constant temperature of 20 ^{0}C by water cooling during the experiments. The schematic of the initial short x-cavity is presented in Fig. 4.1.1.

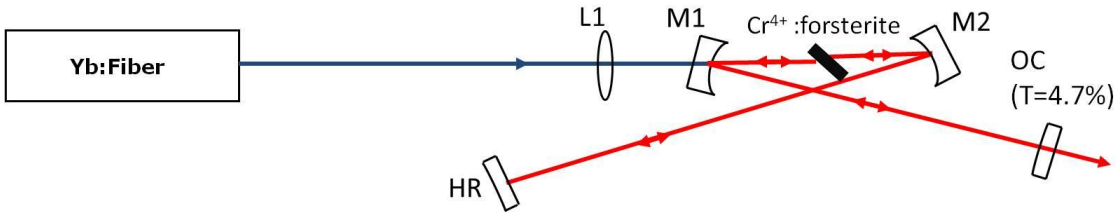

Figure 4.1.1 *The schematic of the short x-cavity* Cr^{4+}: forsterite laser.

In addition, a flat DCM high reflector (HR) and a flat output coupler (OC) with 4.7 % transmission were used for the construction of the x-cavity. The output coupler and high reflector arm lengths were 50.5 cm and 43.5 cm respectively. From this configuration, an average output power of 815 mW was obtained with 8 W input pump power in continuous wave operation.

In order to reduce the repetition rate of the short cavity and scale the pulse energy, the short cavity was extended by incorporating a q-preserving multi-pass cavity (MPC). Before the addition of the MPC, HR mirror was removed. Two flat DCM mirrors (M3 and M4) were added to the x-cavity for adjusting the inclination angle of the beam entering the MPC. Figure 4.1.2 (a) shows a photograph of the x-cavity with M3 and M4. The schematic of the x-cavity and MPC is presented in Fig. 4.1.2 (b).

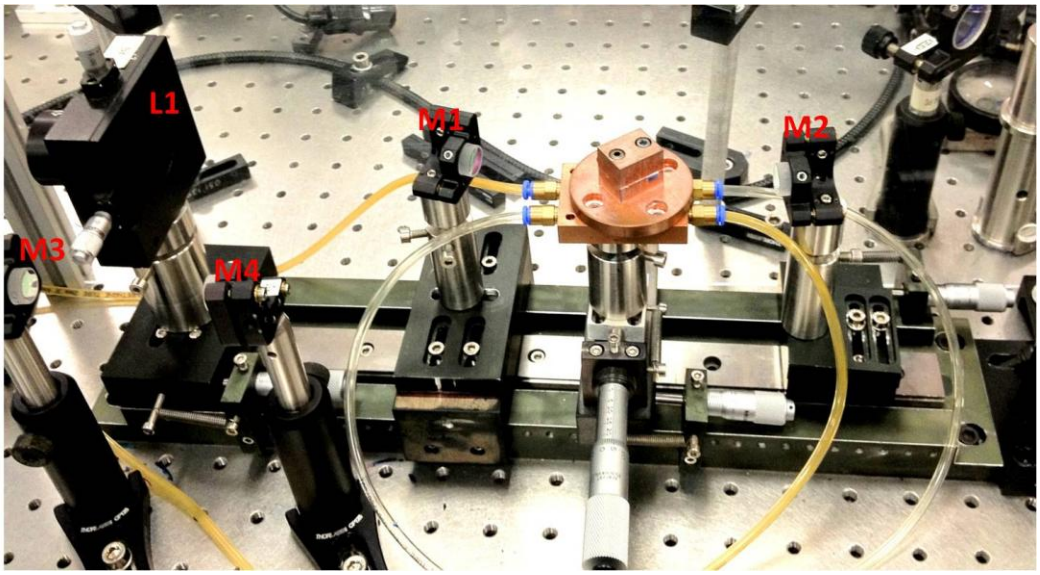

Figure 4.1.2 (a) *The short cavity with the mirrors M3 and M4.*

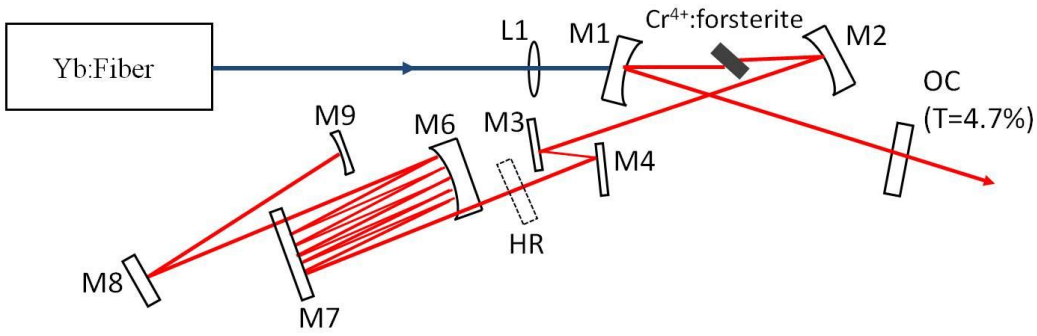

Figure 4.1.2 (b) *The extension of the short x-cavity with the multi-pass cavity.*

The MPC contained a curved mirror (M6) with a 4 m RC and a flat mirror (M7). In order to allow beam injection and extraction, both of the mirrors had notches. The laser beam completed n=9 round-trips inside the MPC and the integer value m was equal to 4. From

Eq. (3.2.34), the required separation between the mirrors M6 and M7 was set to 165 cm. For this separation, the angular advance of the circular spot pattern was 80^0 per round-trip. To maintain the q-preserving condition, the exciting beam was retro-reflected with a curved end mirror (M9) located at a distance of 165 cm from M7 and with RC = 2m. RC was chosen according to the q-preserving condition given in Eq. (3.2.34) for MPC mirrors with notches [48]. In Fig. 4.1.3 images of the spot patterns on both M6 and M7 can be seen.

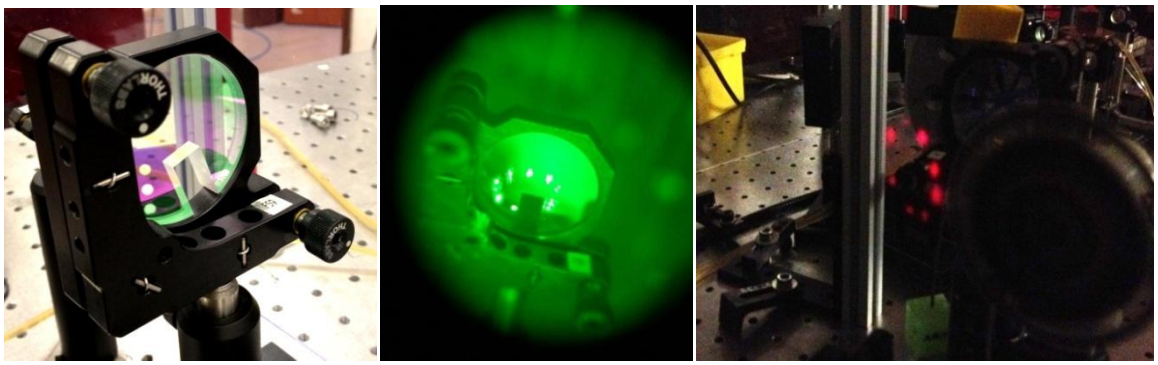

Figure 4.1.3 (a) *Image of the flat MPC mirror M7.****(b)*** *Green colored digital image shows the spot pattern on the flat MPC mirror M7,taken with an infrared viewing camera. (courtesy of H. Cankaya).* ***(c)*** *The second digital image was taken with the help of a rotating IR- sensitive card connected to a chopper. The system was built by S. Ozharar. This system was put in front of M6 and created an image of the spot pattern as the bouncing beam scattered from the IR-sensitive card.*

As a result, the MPC added an effective optical path length of 59.4 m to the short cavity without perturbing the q-parameter of the original laser beam. With this configuration, the overall cavity produced 670 mW average output power from 8 W input pump power.

In the third step of experimental design, another x-cavity was built to create a beam waist for saturating the saturable absorbers used in our experiments. As described in Chapter 3, to compensate the self-phase modulation effects coming from the cavity nonlinearities,

DCM and GTI mirrors were used to build the second x-cavity. In this part, four GTI mirrors (M11, M12, M17, M18) each with -250 fs^2 GDD (group delay dispersion), and three DCMs (M13, M14, M19) each with -150 fs^2 GDD were used. As seen from the schematic description in Fig. 4.1.4 (a), to maximize the total negative dispersion, the beam reflected four times from each GTI mirror. Figure 4.1.4 (b) shows the image of the final experimental setup. In addition to this, to increase the pulse energy, OC was placed such that, the total effective transmission was about 9.4 %. The distances between mirrors M1-M15 (133.5 cm), M15-M16 (58.5 cm), and M16-OC (90 cm) were carefully chosen to preserve the mode-matching condition of the original cavity.

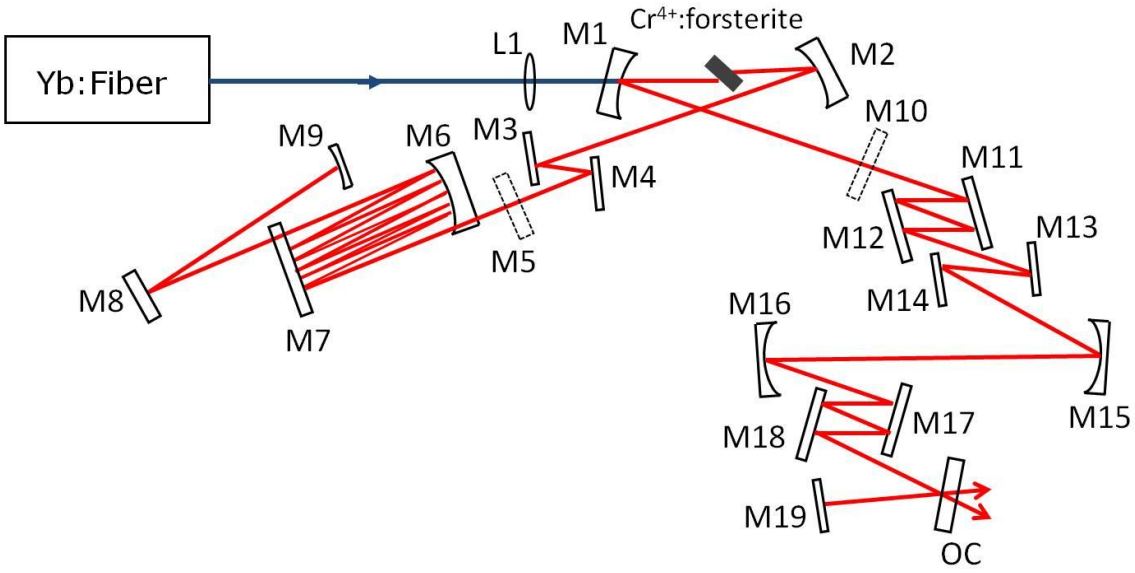

Figure 4.1.4 (a) *Schematic of the experimental set-up with the multi-pass cavity and dispersion control optics.*

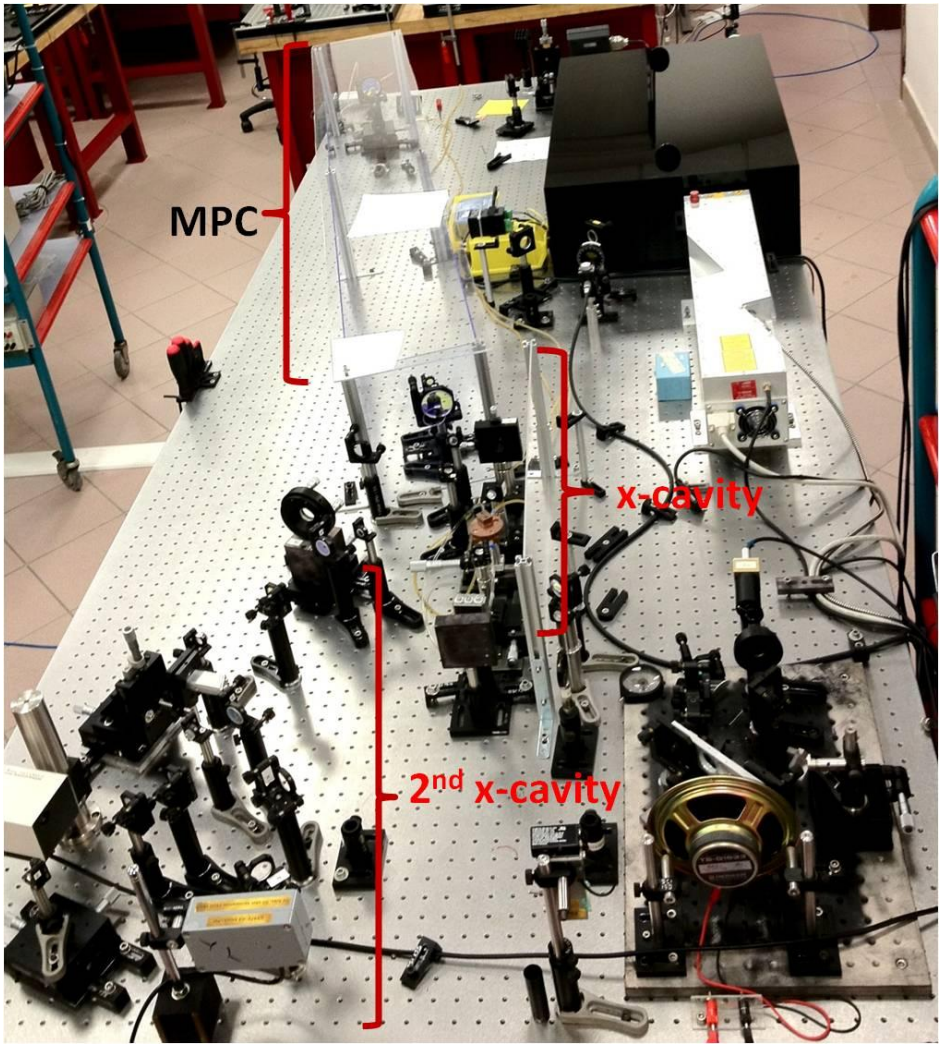

Figure 4.1.4 (b) *Image of the final experimental setup.*

With the help of two curved mirrors M16 and M17 each with radius of curvature 50 cm, an estimated waist of 97 μm was obtained at the location of the saturable absorber. The total negative dispersion due to four GTI mirrors and eight DCMs was around -6400 fs^2. After accounting for the positive dispersion due to the crystal (+800 fs^2), MPC (+360 fs^2), quartz

substrate of SWCNT-SA / graphene-SA (+7 fs^2), and air (+794 fs^2), the net GDD of the cavity was estimated to be around -4440 fs^2. With this final configuration, 495 mW of average output power was obtained in continuous regime at the input pump power of 8 W. The effective output coupling was 9.4 %. For 4.7 % transmitting output coupler, the output power was 625 mW with the same input pump power. As a result, with the MPC extension and dispersion control optics (DCO), the repetition rate of the short cavity was reduced to 4.51 MHz from 144 MHz (Eq. (2.2.9)).

With the addition of the SWCNT-SA or the graphene-SA, the efficiency of the laser was reduced due to the losses coming from the saturable absorber. Figure 4.1.5 shows the overall efficiency data for all components with SWCNT-SA and graphene-SA.

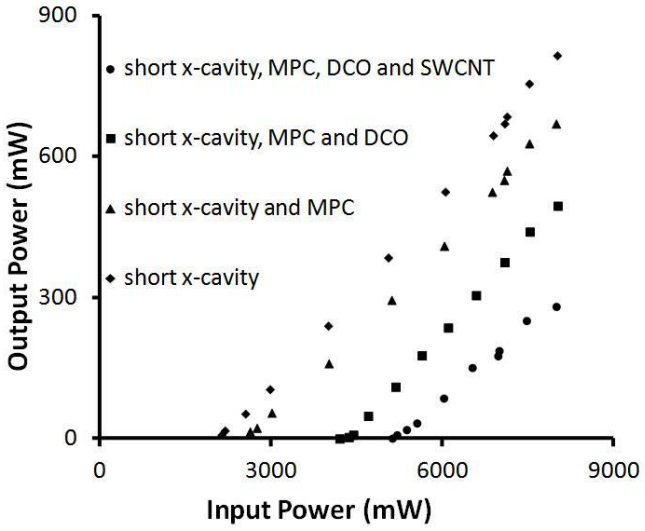

Figure 4.1.5 (a) *Efficiency data for the different cavity configurations and final configuration with SWCNT-SA and 9.4 % effective output coupling.*

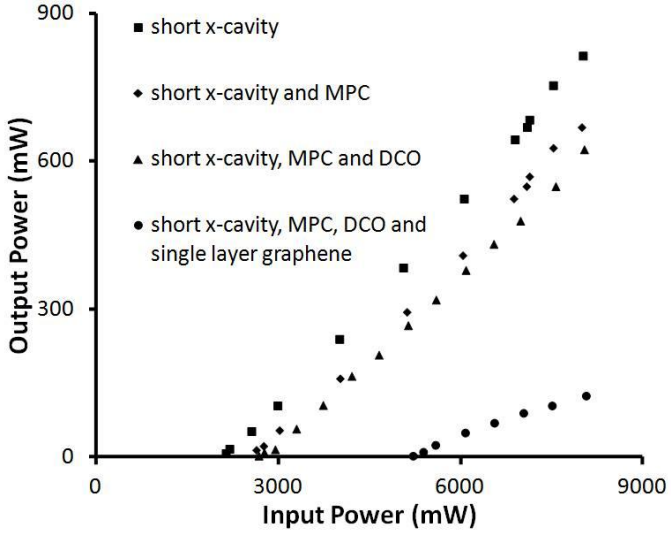

Figure 4.1.5 (b) *Same efficiency data but the final configuration consists of a single layer graphene-SA with 4.7 % effective output coupling.*

The passive loss of the Cr^{4+}: forsterite crystal was around 3.14 %. From the efficiency data and threshold power analysis described in Eq. (1.2.39), the passive losses for the MPC, DCO, SWCNT-SA, and graphene-SA were estimated to be 1.72 %, 0.8 %, and 3.76 %, and 6 %. The efficiencies for each configuration were, 13.7 %, 12.4 %, 13.4 % (for 9.4 % OC), 11.5 % (for 4.7 % OC) and 10.2 %, 4 %, respectively. Note that, the passive losses for SWCNT-SA and single layer graphene-SA were measured during continuous wave regime and these losses are approximately the sum of saturable, and non-saturable losses. In the mode-locking regime, these passive losses were somewhat reduced by the saturable losses.

4.2 Mode-locked operation results with SWCNT-SA

The SWCNT-SA was placed at the 97 μm beam waist between mirrors M15 and M16 as shown in Fig. 4.2.1. With this beam waist, an incident fluence of 368 μJ /cm^2 was achieved. This incident fluence was sufficient to start mode-locking operation and it was small enough to prevent two-photon absorption [49].

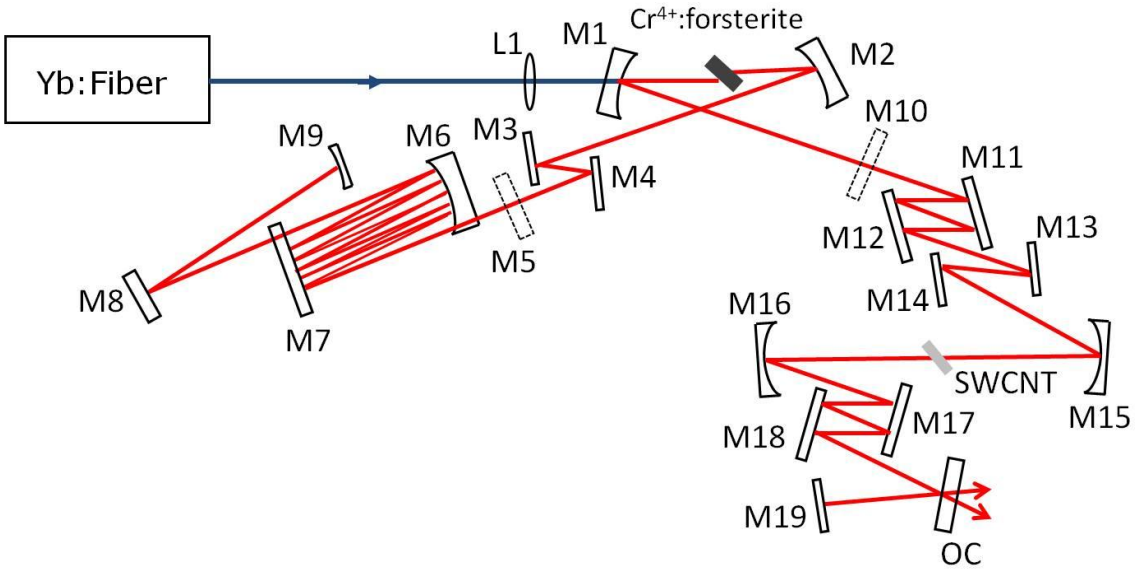

Figure 4.2.1 *Schematic showing the location of the SWCNT-SA in the experimental set-up.*

The SWCNT sample was synthesized by our co-workers using high-pressure CO conversion technique (HiPCO), and then SWCNTs were mixed with a polymer called polymethylmethacrylate (PMMA). The mixture containing SWCNT and PMMA was placed on an optically polished 1mm thick quartz substrate. Details for the fabrication can be found in reference [49]. Figure 4.2.2 shows the image and transmission spectrum of the

SWCNT-SA sample used in our experiments. The relaxation time of SWCNT-SA was less than 2 ps with 10 μJ /cm^2 saturation fluence and 0.5 % modulation depth [49].

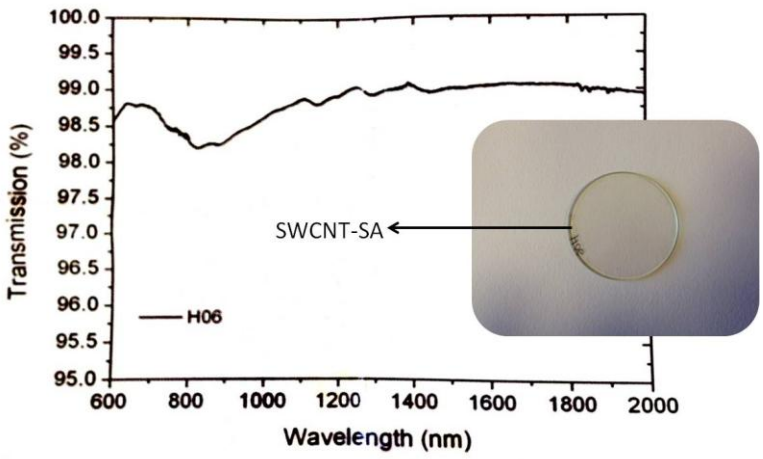

Figure 4.2.2 *The image of the SWCNT-SA used in our experiments (inset). Transmission spectrum of the SWCNT-SA. The transmission spectrum shows an absorption band near 1250 nm.*

As a result, by using the SWCNT-SA, mode-locked operation of Cr^{4+}: forsterite laser at 1247 nm was achieved. The spectral width of the mode-locked spectrum was 16 nm with 121 fs pulse duration, and with a time-bandwidth product of 0.37. This suggests that the transform-limited pulses had a temporal profile close to that of a $sech^2$ pulse. The mode-locked spectrum and autocorrelation trace can be seen in Fig. 4.2.3.

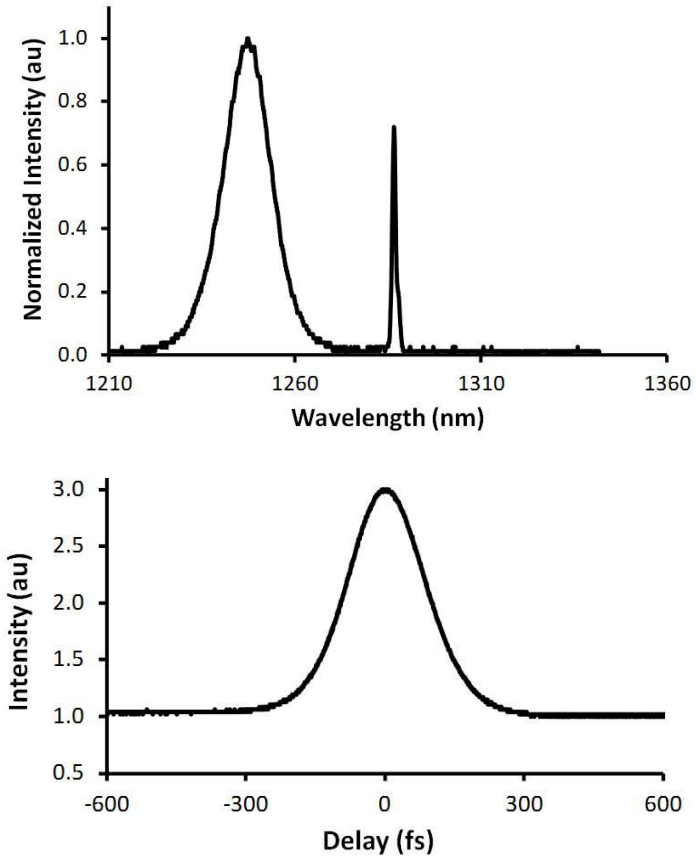

Figure 4.2.3 (a) *The spectrum and* ***(b)*** *the collinear autocorrelation data for the mode-locked* Cr^{4+}*: forsterite laser. The continuous wave peak in the spectrum around 1290 nm is believed to be due to GDD oscillations of the GTI mirrors.*

To measure the pulse width, we used a collinear autocorrelator and a fast Si detector. The schematic description and explanation of the autocorrelator is presented in Fig. 4.2.4.

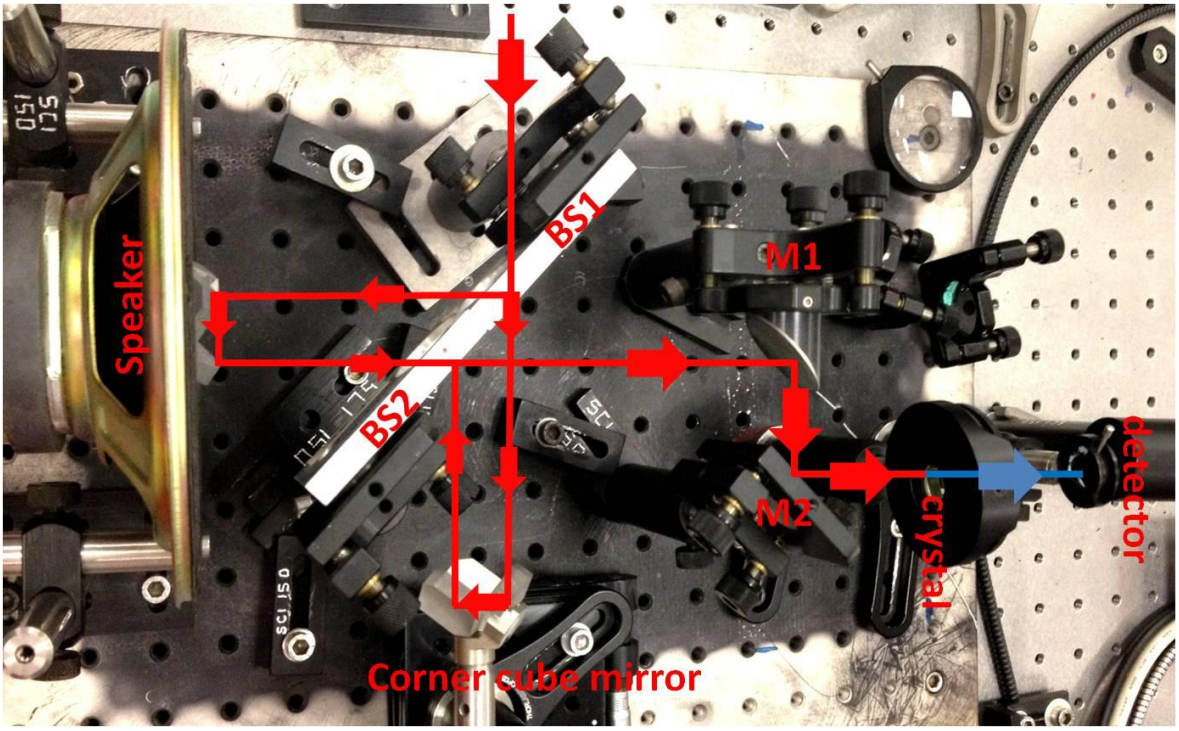

Figure 4.2.4 *A schematic for the collinear autocorrelator setup. This setup is similar to an interferometer. The beam coming from the output of the* Cr^{4+}*: laser is split into two parts. One beam travels without time delay, whereas the other beam is delayed with the help a mirror connected to an externally driven speaker. Two beams are combined with the help of the second beam splitter (BS2) and they travel to the nonlinear crystal through M1 and M2. The mode-locked signal generates second harmonic (*λ_{source} */ 2) of the laser wavelength inside the nonlinear crystal. By using the corner cube mirror, the interval where the arm lengths of the autocorrelator are equal can be searched. When two arm lengths are equal to each other, as a result of the interference, autocorrelator signal is obtained.*

With the SWCNT-SA, an average output power of 280 mW was achieved at the input power of 8 W in the continuous wave regime, by using an output coupler with an effective transmission around 9.4 %.

Stable mode-locked operation was obtained with an average output power of 46 mW. Any further increase in the output power resulted in multi-pulsing instabilities. With this average output power and 4.51 MHz repetition rate, 10 nJ of pulse energy was obtained. The corresponding intracavity pulse energy was 108.5 nJ and the intracavity peak power was 0.9 MW. The peak power of the pulses was 84 kW, which is the highest peak power obtained from a bulk solid-state femtosecond laser mode-locked with SWCNT-SA [17].

Using the soliton-area theorem given by Eq. (3.1.12), the nonlinear refractive index of the Cr^{4+}: forsterite crystal (n^g_2) was calculated. For the calculations, nonlinear coefficients of both air and crystal were calculated by expanding Eq. (3.1.11)

$$\gamma_{net} = \gamma_g + \gamma_{air} \tag{4.2.1}$$

where γ_g is the nonlinear coefficient for the Cr^{4+}: forsterite crystal and γ_{air} is for the nonlinear coefficient of air. They are given by Eq. (3.1.11) as

$$\gamma_{net} = \frac{2\pi}{\lambda}\left(n_2^g \frac{2l_g}{A_{eff}^g} + n_2^{air} \frac{2l_{air}}{A_{eff}^{air}}\right). \tag{4.2.2}$$

In Eq. (4.2.2), l_g and l_{air} are the distances travelled by the laser beam in the crystal and in air, respectively. A^g and A^{air} are the effective areas of the laser beam in the crystal and in air. Although the laser beam travels a large distance in air (~ 60 m), nonlinearity of air at 1247 nm is small compared to that of the crystal [50]. Hence, the nonlinear coefficient for air was neglected in our calculations. As a result, by using Eq. (4.2.2) and Eq. (3.1.12), the nonlinear refractive index of the Cr^{4+}: forsterite crystal was calculated as 9.36 x 10^{-20} m^2 / W. This n_2 value is in reasonable agreement with the n_2 value (6 ± 4 x 10^{-20} m^2 / W) reported by Chassagne et al. [51]. With this n_2 value and by using Eq. (3.1.9), the critical power for

self-focusing was calculated as 1.5 MW inside the cavity. Our experimental value of 0.9 MW was in a reasonable agreement with the calculated critical power. As described above, any further increase in the output power caused mode-locking instabilities. In order to test this limit, we changed our output coupler transmission to 4.7 % from 9.4 %. In this case, 5 nJ pulse energy was obtained with the same intracavity peak power of 0.9 MW. Above this limit, again mode-locking instabilities occurred. By changing the output coupler, output power of the laser was increased (at 7.1 W input pump power, output power was 295 mW for 4.7 %, 210 mW for 9.4 % transmission, with SWCNT-SA) since it was near to the optimum output coupler transmission point for our cavity as can be seen in Fig. 4.2.5.

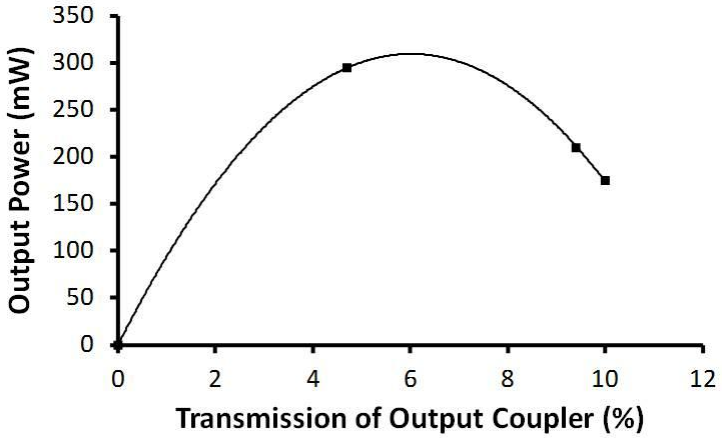

Figure 4.2.5 *The output power of the Cr^{4+}: forsterite laser as a function of different output coupler transmissions.*

As a result, we obtained mode-locked operation of Cr^{4+}: forsterite laser by using a SWCNT-SA. The laser was operated at room temperature and produced 121 fs transform-limited pulses at 1247 nm with 16 nm spectral width. The pulse energy was 10 nJ, and the corresponding peak power was 84 kW, which is the highest peak power reported for a bulk

femtosecond laser mode-locked with a SWCNT-SA. Further increase in pulse energy can be obtained by increasing the transmission of the output coupler. However, in our case output coupler transmissions beyond 11 % did not worked as seen in Fig. 4.2.5. In addition to this, it was shown that any further increase in the peak power is only limited due to the cavity nonlinearities. This suggests that it could be possible to further increase the peak power of other types of laser systems by using SWCNT-SAs if the gain medium has smaller Kerr nonlinearity.

4.3 Mode-locked Operation Results with Graphene-SA

For the mode-locking experiments with graphene-SA, the same laser architecture was used as in Fig. 4.2.1. The only difference was the transmission of the output coupler. As described in Chapter 2, each graphene layer has nearly 2.3 % absorption over the optical spectrum given in Eq. (2.3.4). Hence, with 9.4 % output coupler transmission and loss of single layer graphene-SA, it was not possible to operate our Cr^{4+}: forsterite laser as explained in Fig. 4.2.4. Therefore, a 4.7 % output coupler was used during the experiments with a single layer graphene-SA. The image of the dispersion control optics cavity can be seen in Fig. 4.3.1. The graphene-SA was placed at approximately the same waist of 97 μm. This gives 383 $\mu J/cm^2$ incident fluence on the graphene-SA. The images for the graphene-SA samples and the transmission spectrum of the graphene-SAs used in our experiments can be found in Fig. 4.3.2.

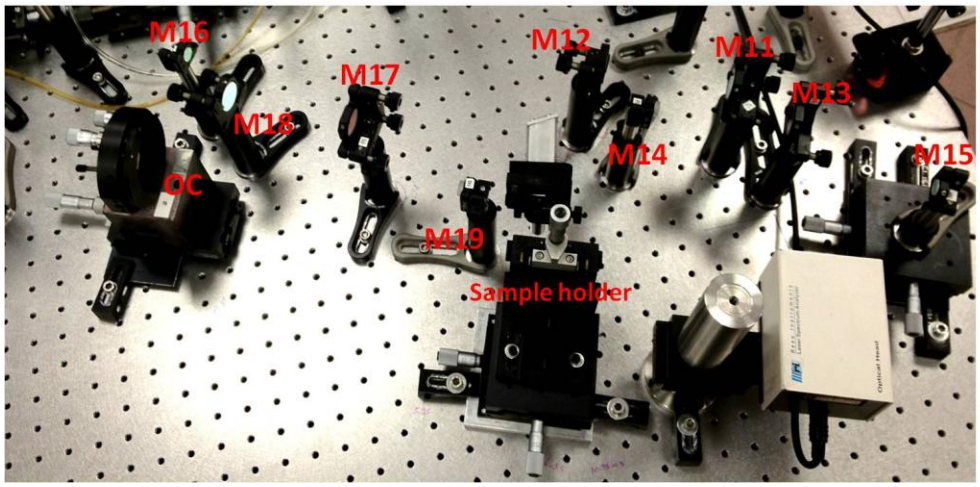

Figure 4.3.1 *An image of the second x-cavity which is composed of dispersion control optics. For SWCNT-SA experiments, we changed the locations of OC and M19 to have 9.4 % effective output coupling which can be seen in Fig.4.2.1.*

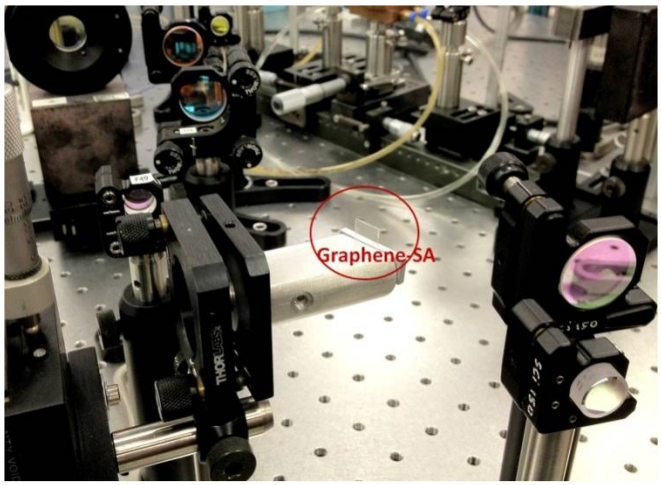

Figure 4.3.2 (a) *Image of the graphene-SA sample used in our mode-locking experiments.*

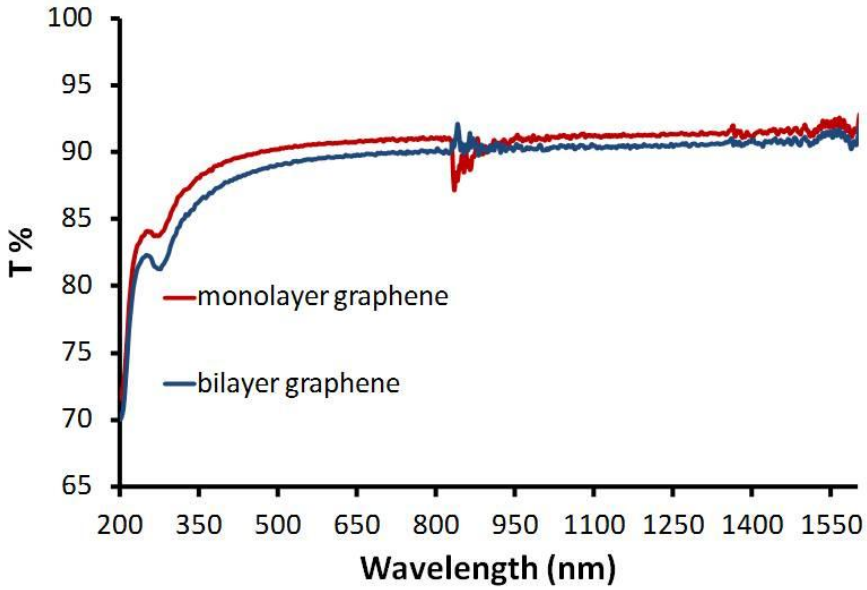

Figure 4.3.2 (b) *The transmission spectra for monolayer and bilayer graphene. As explained in Chapter 2.3.2, graphene has nearly flat absorption band which covers a wide range of the electromagnetic spectrum in the visible and near infrared. In addition, the characteristic peak of graphene around UV region can be seen from the transmission spectra.*

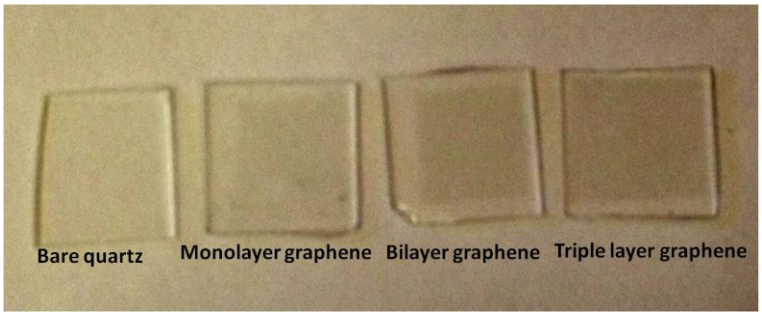

Figure 4.3.2 (c) *Image showing the different number of graphene layers on a quartz substrate. From Eq. (2.3.4) and the spectrum in Fig. 4.3.2 (b), it is obvious that the number of layers affects the absorption strength of graphene.*

Raman spectra have been used for characterizing the graphene [52]. The Raman spectrum is based on the Raman scattering process which is an example of inelastic scattering and discovered by Sir Chandrasekhara Venkata Raman. In the Raman effect, there are two processes called stokes and anti-stokes scattering that are shown in Fig. 4.3.3. In Raman scattering, one photon is scattered inelastically by the crystal which results in the creation (stokes process) or annihilation (anti-stokes process) of a phonon.

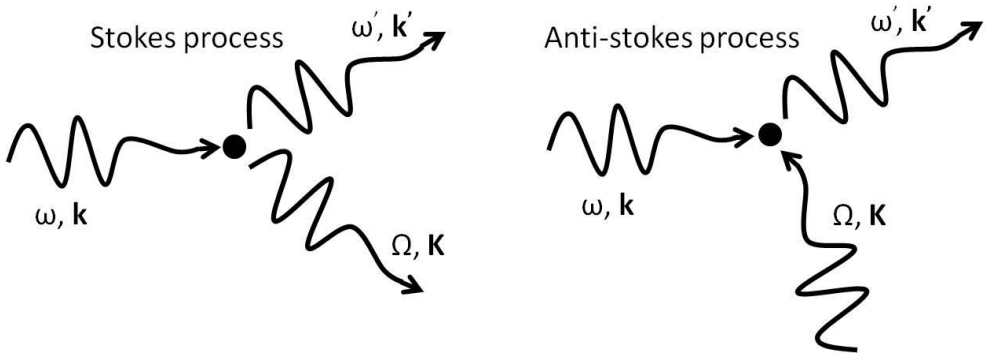

Figure 4.3.3 *Stokes and anti-stokes processes of Raman scattering. (adopted from C. Kittel,Introduction to Solid State Physics)*

In Fig. 4.3.3, ω and ω' stand for angular frequencies of incident and scattered photons. Similarly, **k** and **k'** are the corresponding wave vectors of the incident and scattered photons. Ω and **K** are the angular frequency and wave vector of created or annihilated phonon. The Raman spectrum is related with the excitation of the optical phonons in the crystal structure. In Fig. 4.3.4 the Raman spectrum of the graphene-SA used in our experiments is presented.

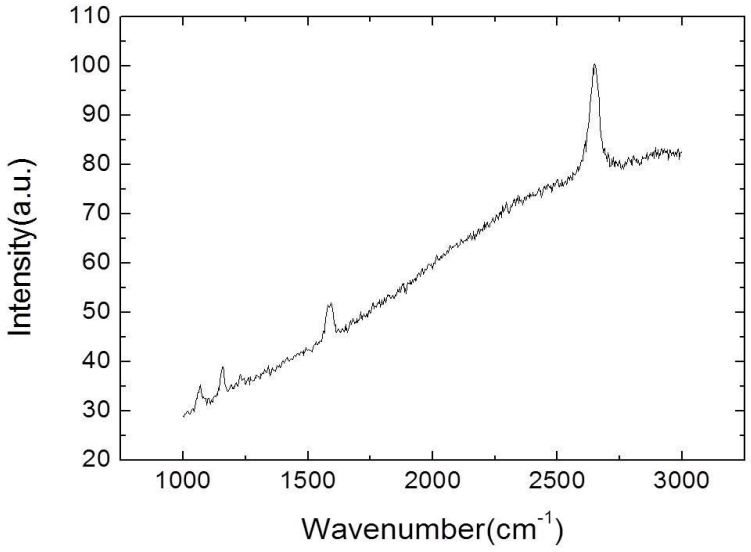

Figure 4.3.4 *Raman spectrum of the graphene-SA. (Raman spectrum was taken by C. Kocabas, and E. Pince at Bilkent University, by using a 532 nm laser source)*

In this figure, the large amount of background noise is due to the quartz substrate where graphene was deposited on. The first band near 1350 cm^{-1} is called D-band (defect mode) and it is due to the defects of the graphene. When the photon hits a defect, it undergoes stokes or anti-stokes process and results in the creation or annihilation of one phonon, which generates the D-band. D-band should be sharp but it should be less intense than the other peaks, because it gives the amount of impurities in the graphene sample. (the other band near 1000 cm^{-1} is due to impurities in quartz substrate). The second band near 1500 cm^{-1} is known as the G-band and it is due to the presence of the lattice formed by the carbon atoms. It results from the in-plane and out-of-plane phonon vibrations of the graphene lattice. If the incident photon couples with the in-plane phonon vibrations of the graphene lattice, one phonon is created or annihilated due to this coupling and the G-band

is observed. The G-band should be more intense than the D-band. The last band near 2500 cm^{-1} is known as the 2D-band. It is placed at a point which is two times greater than the D-band. That's why it is known as the 2D-band by convention. However, it is not due to the defects of graphene. It is a second-order process which is similar to the process for the G-band. In this process, two phonons are created or annihilated due to the photon-phonon coupling. In our Raman spectrum, we are not dealing with negative wavenumbers hence, we can say that only the Stokes process is observed in this Raman spectrum. Therefore, due to this process, phonons are created and not annihilated. The 2D-band should be the most intense and sharpest peak, because if we go from single layer graphene to the graphite structure, the 2D-band becomes larger [53]. D / G, and G / 2D ratios characterize the graphene. D / G ratio gives the amount of defects in the graphene. G / 2D ratio gives information about the layers of the graphene. In addition to this, the width (FWHM) of the 2D-band also gives information about the number of layers. For our sample, FWHM of the 2D-band was equal to 42.08 cm^{-1}.

These peaks in the Raman spectrum are fingerprints of graphene. However, it is not possible to say that a graphene sample is exactly single layer by only considering the Raman spectrum. The 2D-band and the G-band are due to vibrations in the graphene lattice and give information about the number of layers. Nevertheless, bilayer graphene can give similar spectrum with single layer graphene. Two layers of graphene can act as one isolated single layer and give a similar Raman spectrum. Therefore, it is more convenient to say that we have a few layer graphene, but we can accept our sample as a single layer graphene because from the transmission spectrum we can understand that absorption of the single layer of graphene was about 2 % which is consistent with Eq. (2.3.4). The graphene-SA sample was fabricated in Asst. Prof. Coskun Kocabas's laboratory at Bilkent University, with the help of Ph.D students Osman Balci, and Ercag Pince. In the synthesis process, we used CVD (chemical vapor deposition) technique to grow graphene layers on a high purity

Cu substrate. Details of the process can be found in a similar article [54]. In Fig. 4.3.5, the furnace used for graphene synthesis is shown.

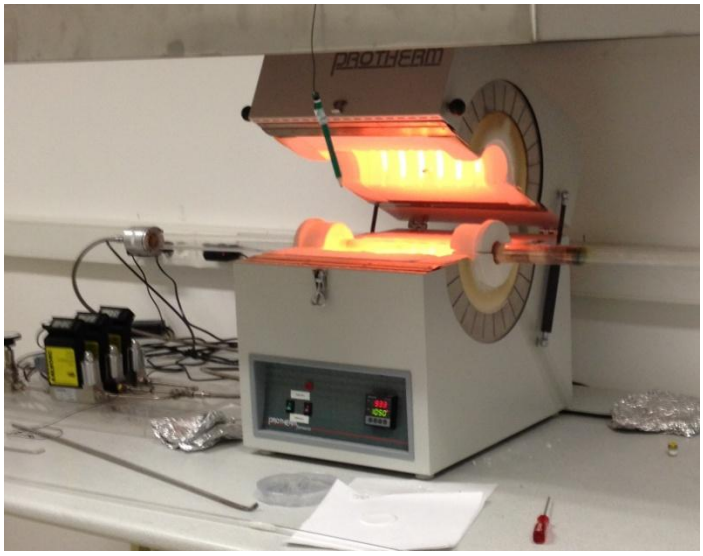

Figure 4.3.5 *The furnace used for graphene synthesis on Cu substrate (at 1000 ^{0}C). In this process Ar, H and CH_4 gases were used. CH_4 was chosen as the carbon source for graphene.*

After graphene was grown on a Cu substrate, this combination was coated with a photoresist by using spin coater. Then, at this stage we had Cu with graphene and on top of them we had photoresist. This configuration was then pasted to a polymer structure called polydimethylsiloxane (PDMS). This structure is described in Fig. 4.3.6. Then, to solve Cu substrate, this it was put in a Fe(III)Cl_3 solution which can be seen in Fig. 4.3.6. After Cu was dissolved, we had PDMS + photoresist + graphene layer with the same order as in Fig. 4.3.6. At the final stage, the structure was pasted onto an optically polished 1mm thick quartz substrate and the photoresist was removed by using acetone. The image of the final structure of graphene-SA can be seen in Fig. 4.3.2 (c).

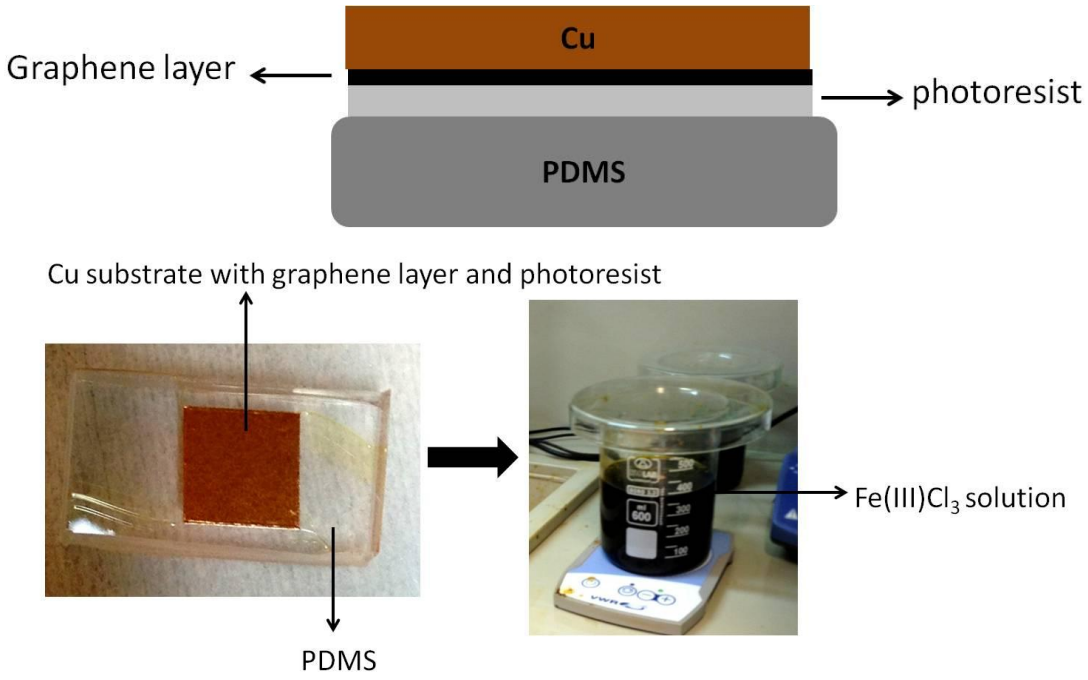

Figure 4.3.6 (a) *The schematic of the layered structure consisting of PDMS, photoresist, graphene layer, and Cu substrate structure.* ***(b)*** *Image of the structure and solution used to remove the Cu substrate.*

As a result, we synthesized a graphene-SA for our mode-locking experiments. The experiments were performed as described at the beginning of this section, with the same configuration as shown in Fig. 4.2.1.

With the addition of the graphene-SA, the efficiency of the Cr^{4+}: laser was considerably reduced. This decrement was due to the non saturable losses of the graphene-SA. The measured efficiency graph can be seen in Fig. 4.1.5.

By using the graphene-SA, mode-locked operation of the Cr^{4+}: forsterite laser operating at 1252 nm was achieved. With the 4.7 % output coupler and 24 mW average output power,

pulses with 5.3 nJ energy and 4.51 MHz repetition rate were obtained. The corresponding peak power of the pulses was 55 kW. This peak power result is higher than the previously reported results for solid-state lasers mode-locked with graphene-SA [39]. Furthermore, the mode-locked spectrum had a 18.2 nm spectral width and the pulse duration was 96 fs, which gives a time-bandwidth product of 0.336. These results show that, nearly-transform limited pulses were obtained with a temporal profile of $sech^2$. The mode-locked spectrum and autocorrelation trace can be found in Fig. 4.3.7.

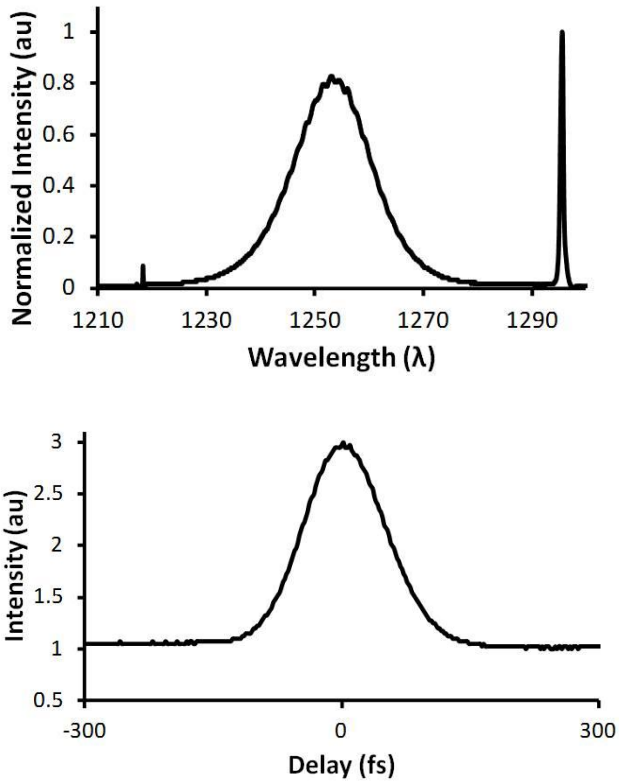

Figure 4.3.7 (a) *Mode-locked spectrum of the Cr:forsterite femtosecond pulses obtained by using the graphene-SA.* ***(b)*** *Collinear autocorrelation trace for the 96 fs pulses. Autocorrelation measurements were done by using the same autocorrelator.*

The intracavity pulse energy was about 112.8 nJ and the corresponding intracavity power was 1.17 MW. Similar to SWCNT-SA mode-locking results, multi-pulsing occured at average output powers greater than 50 mW. In conlusion, graphene-SA results are consistent with the critical power obtained from SWCNT-SA experiments and Eq. (3.1.9).

CHAPTER 5

CONCLUSIONS and POSSIBLE FUTURE STUDIES

In this thesis, a brief background behind the principles of laser operation in the CW and mode-locked regimes was presented. In addition, important characteristics of third-order optical nonlinearities and saturable absorbers were given. Furthermore, design parameters for multi-pass cavities and fabrication details of SWCNT-SA and graphene-SA were described.

During this research, the Cr^{4+}: forsterite laser with different resonator architectures was built step by step and mode-locked operation was demonstrated with two kinds of nano structured carbon based saturable absorbers (SWCNT-SA, graphene-SA). The pulse energy was scaled by incorporating a q-preserving MPC. In order to control the overall positive dispersion inside the resonator, DCMs and GTIs were used and the net dispersion of the resonator was estimated to be around – 4440 fs^2.

The SWCNT-SA sample was prepared by Rotermund et al. by using HiPCO technique as described in reference [49]. The SWCNT-SA introduced a passive loss of 3.76 % to our resonator design with 4.7 % effective output coupling. The Cr^{4+}: forsterite laser mode-locked by using SWCNT-SA produced solitary pulses with a pulse energy around 10 nJ with a 84 kW peak power and a pulse duration about 121 fs. For 16 nm spectral width, the corresponding time-bandwidth product was 0.37.

For the mode-locking experiments with graphene-SA, different graphene-SA samples with different layer thicknesses were fabricated and characterized. These samples were prepeared by Kocabas et al. [54] by using chemical vapor deposition technique

(CVD).Since passive loss of the single layer graphene-SA is higher than SWCNT-SA, resonator was operated with a different effective output coupling (% 9.4). The Cr^{4+}: forsterite laser mode-locked with single layer graphene-SA produced nearly transform-limited solitary pulses with a time-bandwidth product of 0.33. The corresponding spectral width and pulse duration were about 18.2 nm and 96 fs respectively. The pulses had energy around 5 nJ with a 55 kW peak power.

Both of these saturable absorbers produced the highest peak powers obtained from a bulk femtosecond solid-state laser mode locked with SWCNT-SA or graphene-SA.

Furthermore, these mode-locking results were used to determine the n2 value of the Cr^{4+}: forsterite gain medium and it was shown that the only limitation which prevents further increase in the peak power was due to self-focusing based pulsing instabilities. However, this thesis shows that SWCNT-SA and graphene-SA have the potential to be used in initiating mode-locked operation in high-power lasers.

As a future work, the laser efficiency with graphene-SA can be increased. Mode-locking trials will be done by using bilayer and triple layer graphene-SAs if the passive non-saturable losses can be minimized. Moreover, stable mode-locked operation was possible only for about 15 - 20 minutes due to the poor mechanical stability of the mirror mounts. By using improved opto-mechanical hardware, this stability time will be maximized to enable applications by using the Cr^{4+}: forsterite laser.

BIBLIOGRAPHY

1. T. H. Maiman, "Stimulated optical radiation in ruby" Nature **187,** 493 (1960).
2. E. M. Callaway and R. Yuste, "Stimulating neurons with light" Curr Opin Neurobiol **12,** 587 (2002).
3. N. I. Smith, "Biophotonics: A light to move the heart" Nature Photonics **4,** 587 (2010).
4. T. Wu., N. A. Timo, S. Mohanty, J. Miotke, R. L. Meyer, H. Rubinsztein-Dunlop, and M. W. Berns, "A photon-driven micromotor can direct nerve fibre growth" Nature Photonics **6,** 62 (2012).
5. F. E. Goodwin, "A review of operational laser communication systems" IEEE **58,** 1746 (1970).
6. T. Steinmetz, T. Wilken, C. A. Hauck, R. Holzwarth, T. W. Hansch, L. Pasquini, A. Manescau, S. D'Odorico, M. T. Murphy, T. Kentischer, W. Schimidt, and T. Udem, "Laser Frequency Combs for Astronomical Observations" Science **5,** 1335 (2008).
7. A. J. Lee and D. P. Casasent, "Computer generated hologram recording by using a laser printer" Appl. Opt. **26,** 136 (1987).
8. X. Liu, D. Du, and G. Mourou, "Laser ablation and micromachining with ultrashort laser pulses" IEEE J. Quantum Electron. **33,** 1706 (1997).
9. A. Sennaroglu, *Photonics and Laser Engineering* (Mc Graw-Hill).
10. V. Petricevic, S. K. Gayen, R. R. Alfano, K. Yamagishi, H. Anzai, and Y. Yamaguchi, "Laser action in chromium-doped forsterite" Appl. Phys. Lett. **52,** 1040 (1988).
11. A. Seas, V. Petricevic, and R. R. Alfano, "Continuous-wave mode-locked operation of a chromium-doped forsterite laser" Opt. Lett. **16,** 1668 (1991).
12. W. Jia, H. Liu, S. Jaffe, and W. M. Yen, "Spectroscopy of Cr^{3+} and Cr^{4+} ions in forsterite" Phys. Rev. B. **43,** 5234 (1991).
13. M. J. Colles and a. C. R. Pidgeon, "Tunable Lasers" Rep. Prog. Phys. **38,** 329 (1975).
14. C. Chudoba, J. G. Fujimoto, E. P. Ippen, H. A. Haus, U. Morgner, F. X. Kaertner, V. Scheuer, G. Angelow, and T. Tschudi, "All-solid-state Cr:forsterite laser generating 14-fs pulses at 1.3 μm" Opt. Lett. **26,** 292 (2001).
15. A. Sennaroglu, "Efficient Continuous-Wave Radiatively Cooled Cr 4 :Forsterite Lasers at Room Temperature" Appl. Opt. **37,** 1062 (1998).

16. H. Cankaya, A. Sennaroglu, and S. Akturk, "Direct generation of 81 nJ pulses and external compression to a subpicosecond regime with a 4.9 MHz chirped-pulse multipass-cavity Cr(4+):forsterite oscillator" Opt. Lett. **36,** 1572 (2011).
17. I. Baylam, S. Ozharar, H. Cankaya, S. Y. Choi, K. Kim, F. Rotermund, U. Griebner, V. Petrov, and a. A. Sennaroglu, "Energy scaling of a carbon nanotube saturable absorber mode-locked femtosecond bulk laser" Opt. Lett. **37,** 3555 (2012).
18. R. C. Stoneman, "Eye Safe Rare Earth Solid-State Lasers," in *Solid-State Lasers and Applications*, A. Sennaroglu, ed. (CRC Press).
19. S. Sakadic, U. Demirbas, T. R. Mempel, A. Moore, S. Ruvinskaya, D. A. Boas, A. Sennaroglu, F. X. Kaertner, and J. G. Fujimoto, "Multi-photon microscopy with a low-cost and highly efficient Cr:LiCAF laser" Opt. Express **16,** 20848 (2008).
20. G. J. Tearney, M. E. Brezinski, B. E. Bouma, S. A. Boppart, C. Pitris, J. F. Southern, and J. G. Fujimoto, "In vivo endoscopic optical biopsy with optical coherence tomography" Science **276,** 2037 (1997).
21. B. C. Young, W. M. Itano, and a. J. C. Bergquist, "Visible lasers with subhertz linewidths" Phs. Rev. Lett. **82,** 3799 (1999).
22. K. Gürs, *Beats and Modulation in Optical Ruby Lasers*, Quantum Electronics III (New York: Columbia Univ. Press).
23. H. S. a. G. L. Tang, *Zeeman Effect and Nonlinear Interactions Between Oscillating Laser Modes*, Quantum Electronics III (New York: Columbia Univ. Press).
24. M. DiDomenico, "Small-signal analysis of internal (coupling type) modulation of lasers" J. Appl. Phys. **35,** 2870 (1964).
25. L. E. Hargrove, R. L. Fork, and a. M. A. Pollack, "Locking of He-Ne laser modes induced by synchronous intracavity modulation" Appl. Phys. **5,** 4 (1964).
26. A. Yariv, "Internal modulation in multimode laser oscillators" J. Appl. Phys. **36,** 388 (1965).
27. B. Furch, "Isolation and frequency conversion properties of acoustooptic modulators" Appl. Opt. **21,** 2344 (1982).
28. U. Keller, K. J. Weingarten, F. X. Kartner, D. Kopf, B. Braun, I. D. Jung, R. Fluck, C. Hönninger, N. Matuschek, and J. Aus. der. Au, "Semiconductor saturable absorber mirrors (SESAM's) for femtosecond to nanosecond pulse generation in solid-state lasers" IEEE J. Sel. Top. Quantum Electron. **2,** 435 (1996).
29. H. A. Haus, "Mode-locking of lasers" IEEE J. Sel. Top. Quantum Electron. **6,** 1173 (2000).

30. P. W. Smith, Y. Silberg, and D. Q. B. Miller, "Mode-locking of semiconductor diode lasers using saturable excitonic nonlinearities" J. Opt. Soc. Am. B **2,** 1228 (1985).
31. P. R. Wallace, "The band theory of graphite" Phys. Rev. **71,** 622 (1947).
32. J. C. Charlier, P. C. Eklund, J. Zhu, and A. C. Ferrari, "Electron and phonon properties of graphene: Their relationship with carbon nanotubes" Top. Appl. Phys. **111,** 673 (2008).
33. R. R. Nair, "Fine structure constant defines transparency of graphene" Science **320,** 1308 (2008).
34. A. B. Kuzmenko, E. V. Heumen, F. E. Carbone, and V. D. Marel, "Universal optical conductance of graphite" Phs. Rev. Lett. **100,** 117401 (2008).
35. F. Bonaccarso, Z. Sun, T. Hasan, and A. C. Ferrari, "Graphene photonics and optoelectronics" Nature Photonics **4,** 611 (2010).
36. I. Sumio, "Helical microtubes of graphitic carbon" Nature **354,** 56 (1991).
37. S. M. Bachilo, M. S. Strano, C. Kitrell, R. H. Hauge, R. E. Smalley, and R. B. Weisman, "Structure-assigned optical spectra of single-walled carbon nanotubes" Science **298,** 2361 (2002).
38. P. Avouris, M. Freitag, and V. Perebeinos, "Carbon-nanotube photonics and optoelectronics" Nature Photonics **2,** 341 (2008).
39. T. Hasan. Z. Sun, and A. C. Ferrari, "Ultrafast lasers mode-locked by nanotubes and graphene" Physica E. (2012).
40. D. Huang, M. Ulman, L. H. Acioli, H. A. Haus, and J. G. Fujimoto, "Self-Focusing-Induced Saturable Loss for Laser Mode-Locking" Opt. Lett. **17,** 511 (1992).
41. J. G. Fujimoto,H. A. Haus, and E. P. Ippen, "Analytic theory of additive pulse and Kerr lens mode locking" IEEE J. Quantum Electron. **28,** 2086 (1992).
42. J. Desbois, F. Gires, and P. Tournois, "A new approach to picosecond laser pulse analysis and shaping" IEEE J. Quantum Electron. **9,** 213 (1973).
43. J. Kuhl, J. Heppner, "Compression of fs optical pulses with dielectric multi-layer interferometers" IEEE J. Quantum Electron. **22,** 182 (1986).
44. R. Szipocs, K. Ferencz, C. Spielmann, and F. Krausz, "Chirped multilayer coatings for broadband dispersion control in femtosecond lasers" Opt. Lett. **19,** 201 (1994).
45. F. X. Kartner, N. Matuschek, T. Schibli, U. Keller, H. A. Haus, C. Heine, R. Morf, V. Scheuer, M. Tilsch, and T. Tschudi, "Design and fabrication of double-chirped mirrors" Opt. Lett. **22,** 831 (1997).
46. V. Shcheslavskiy, F. Noack, V. Petrov, and N. Zhavoronkov, "Femtosecond Regenerative Amplification in Cr:Forsterite" Appl. Opt. **38,** 3294 (1999).

47. D. Herriot, H. Kogelnik, and R. Kompfner, "Off-Axis in Spherical Mirror Interferometers" Appl. Opt. **3,** 523 (1964).
48. A. Sennaroglu, A. M. Kowalevicz, E. P. Ippen, and J. G. Fujimoto, "Compact femtosecond lasers based on novel multi-pass cavities" IEEE J. Quantum Electron. **40,** 519 (2004).
49. W. B. Cho, J. H. Yim, S. Y. Choi, S. Lee, A. Schmidt, G. Steinmeyer, U. Griebner, V. Petrov, D. I. Yeom, K. Kim, and F. Rotermund, "Carbon Nanotubes: Boosting the Non Linear Optical Response of Carbon Nanotube Saturable Absorbers for Broadband Mode-Locking of Bulk Lasers " Adv. Funct. Mater. **20,** 1937 (2010).
50. V. Y. Fedorov and V. P. Kandidov, "A nonlinear optical model of an air medium in the problem of filamentation of femtosecond laser pulses of different wavelengths" Opt. and Spectrosc. **105,** 280 (2008).
51. B. Chassagne, A. Ivanov, J. Oberle, G. Jonusauskas, and C. Rulliere, "Experimental determination of the nonlinear refractive index in an operating Cr:forsterite femtosecond laser" Opt. Commun. **141,** 69 (1997).
52. L. M. Malard, M. A. Pimenta, G. Dresselhaus, and M. S. Dresselhaus, "Raman spectroscopy in graphene" Phys. Rep. **473,** 51 (2003).
53. A. C. Ferrari, J. C. Meyer, V. Scardaci, C. Casiraghi, M. Lazzeri, F. Mauri, S. Piscanec, D. Jiang, K. S. Novoselov, S. Roth, and A. K. Geim, "Raman spectrum of graphene and graphene layers" Phys. Rev. Lett. **97,** 187401 (2006).
54. O. Salihoglu, S. Balci, and C. Kocabas, "Plasmon-polaritons on graphene-metal surface and their use in biosensors" Appl. Phys. Lett. **100,** 213110 (2012).

VITA

Işınsu Baylam was born in Çankaya, Ankara on January 7, 1988. She received her BS degree in Physics from Bilkent University in 2010. In 2010, she was admitted to the Master of Science program in Physics Department at Koç University. Her research interests included femtosecond lasers, solid-state lasers in the near infrared region, biomedical applications of lasers and nonlinear optics. She is a student member of OSA. She will continue her Ph.D. work at Koç University in the same research area.

Publications:

- I. Baylam, S. Ozharar, H. Cankaya, S. Y. Choi, K. Kim, F. Rotermund, U. Griebner, V. Petrov, and A. Sennaroglu, "Energy scaling of a carbon nanotube saturable absorber mode-locked femtosecond bulk laser," *Opt. Lett.*, **37**, 3555-3557 (2012).

Proceedings:

- I. Baylam, S. Ozharar, H. Cankaya, S. Y. Choi, K. Kim, F. Rotermund, U. Griebner, V. Petrov, and A. Sennaroglu, "Energy scaling of a multipass-cavity mode-locked femtosecond bulk laser with a carbon nanotube saturable absorber," SPIE Photonics West (2013) *Laser Source Engineering, Nonlinear Optics, Semiconductor Lasers and LEDs*, February 2-7, San Francisco, California, United States. (submitted)
- I. Baylam, S. Ozharar, H. Cankaya, S. Y. Choi, K. Kim, F. Rotermund, U. Griebner, V. Petrov, and A. Sennaroglu, "Karbon nanotüp doyabilen soğurucular ile 1247 nm dalgaboyunda yüksek enerjili femtosaniye darbe üretimi," Fotonik 2012, 14. Ulusal Optik, Elektro-Optik ve Fotonik Çalıştayı, Eylül 14, Koç University, İstanbul, Türkiye.